Post-fragmentation vesiculation timescales in hydrous rhyolitic bombs from Chaitén volcano

John Browning[1 2*], Hugh Tuffen[3], Mike R James[3], Jacqueline Owen[3], Jonathan M Castro[4], Simon Halliwell[3] and Katia Wehbe[5]

[1]*Departamento de Ingeniería Estructural y Geotécnica, y Departmento de Mineria, Pontificia Universidad Católica de Chile, Santiago, Chile.*

[2]*Centro de Excelencia en Geotermia de los Andes (CEGA, Fondap-Conicyt 15090013), Santiago, Chile.*

[3]*Lancaster Environment Centre, Lancaster University, Lancaster, UK*

[4]*Institute of. Geosciences, University of Mainz, Mainz, Germany*

[5]*Diamond Light Source, Harwell Science and Innovation Campus, Didcot, UK*

*Email: jbrowning@ing.puc.cl

Keywords: Vulcanian explosions, Rhyolite, Chaitén, Vesiculation, Volcanic bombs

Highlights:

- Suite of high temperature bubble growth experiments performed on a rhyolitic bomb from the 2008 eruption of Chaitén volcano
- Hot-stage microscopy allowed the tracing of in-situ bubble growth at different temperatures
- Experimentally derived growth rates placed in context of a cooling volcanic bomb to determine the amount of post-fragmentation vesiculation
- Our model recreates textures observed in metre scale volcanic bombs

ABSTRACT

Bubble nucleation and growth dynamics exert a primary control on the explosivity of volcanic eruptions. Numerous theoretical and experimental studies aim to capture the complex process of melt vesiculation, whereas textural studies use vesicle populations to reconstruct magma behaviour. However, post-fragmentation vesiculation in rhyolitic bombs can create final quenched bubble (vesicle) textures that are not representative of the nature of fragmenting magma within the conduit. To examine bubble growth in hydrous rhyolitic bombs, we have used heated stage microscopy to directly observe vesiculation of a Chaitén rhyolite melt (with an initial dissolved water content of ~0.95 wt. %) at atmospheric pressure and magmatic temperatures upon reheating. Thin wafers of obsidian were held from five minutes up to two days in the heated stage at temperatures between 575 °C and 875 °C. We found that bubble growth rates, measured through changes in bubble diameter, increased with both temperature and bubble size. The average growth rate at the highest temperature of 875 °C is ~1.27 μm s^{-1}, which is substantially faster than the lowest detected growth rate of ~0.02 μm s^{-1} at 725 °C; below this temperature no growth was observed. Average growth rate V_r follows an exponential relationship with temperature, T and inferred melt viscosity η, where $V_r = 5.57\times10^{-7}e^{0.016T}$ and $V_r = 3270.26e^{-1.117\eta}$. Several stages of evolving bubble morphology were directly observed, including initial relaxation of deformed bubbles into spheres, extensive growth of spheres, and, at higher temperatures, close packing and foam formation. Bubble deformation due to bubble-bubble interaction and coalescence was observed in most experiments. We use our simple, experimentally-determined relationship between melt viscosity and bubble growth rates to model post-fragmentation vesicle growth in a cooling 1 m-diameter rhyolitic bomb. The results, which indicate negligible vesicle growth within 2-3 cm of the bomb surface, correspond well with the observed dense margin thickness of a

Chaitén bomb of comparable dimensions. The experiments described can be used to effectively reconstruct the post-fragmentation vesiculation history of bombs through simple analytical expressions which provide a useful tool for aiding in the interpretation of pumiceous endmember textures in hydrous rhyolitic bombs.

Keywords: Bubble growth, Rhyolite, Chaitén, Vulcanian eruptions, Volcanic bombs

1. INTRODUCTION

The nucleation and growth of bubbles in magma exerts a primary control on the dynamics of explosive volcanism (Sparks, 1978). Once bubbles are nucleated in magma, either homogeneously, or heterogeneously on crystal surfaces, they grow by diffusion of molecular volatiles through melt in concert with the decompression and expansion of gas within bubbles. Diffusion produces a volatile concentration gradient that drives continued volatile migration towards a growing bubble (e.g. Toramaru et al., 1989; 1995; Proussevitch et al., 1993). Volatile diffusivity, within a melt, then controls the ability of volatile species to diffuse through the melt into a bubble (e.g. Zhang et al., 1991; Zhang 1999). However growth can be impeded by viscous forces, over natural timescales, in the melt through melt cooling or degassing (e.g. Sparks, 1978; Gardner et al, 1996; Proussevitch and Sahagian, 1996; Navon et al, 1998; Gardner et al, 2000). It has been shown that when viscosity (η) reaches values of $>10^9$ Pa s gas exsolution is hampered and bubble growth is significantly retarded, effectively quenching bubble growth (Thomas et al., 1994; Gardner et al, 2000). This viscous quench is important because it enables supersaturation of magma, producing high internal bubble pressure that can cause explosive magma fragmentation (Gardner et al., 1996).

Bubble nucleation and growth dynamics in explosively erupted volcanic bombs have received comparatively little attention; however, it has been shown that vesiculation does not necessarily cease when pyroclastic material is explosively ejected (Thomas et al. 1994; Kaminsky and Jaupart, 1997). Bubbles in pyroclasts with water contents ~0.4-3.1 wt.% continue to grow through coalescence and diffusional processes at atmospheric pressure (Hoblitt and Harmon, 1993; Giachetti et al., 2010; Wright et al., 2007), as highlighted schematically in Fig. 1. Significant post-fragmentation pyroclast vesiculation may occur if melt viscosity is sufficiently low and clast size sufficiently large such that cooling rates can remain low in pyroclast interiors (Thomas et al. 1994; Soriano et al., 2009; Clarke et al., 2019). Post-fragmentation bubble nucleation, growth and coalescence is likely, hence, to occur in bombs erupted in Vulcanian explosions (e.g. Wright et al. 2007; Castro et al., 2012a; Saubin et al. 2016). These processes continue where cooling is slow, such that clasts remain above the glass transition (Tg) temperature (~600-700°C, for rhyolites, depending on wt. % H_2O) for sufficient time (Giachetti et al., 2010). Tg is a temperature range that marks the transition from a liquid-like to a solid-like state (e.g. Dingwell, 1998; Dingwell and Webb, 1989; Webb, 1997), and is defined either calorimetrically or in terms of a viscosity of 10^{12} Pa s (Stevenson et al., 1995). Given the possibility of post-fragmentation vesiculation in pyroclasts it is important to disentangle the relative contributions of pre- and post- fragmentation vesiculation on final clast textures, in order to interrogate processes occurring in the conduit and in ejected pyroclasts. This is especially relevant to breadcrust bombs and tuffisite veins, where local melt H_2O concentration also appears to strongly affect vesiculation rates (Wright et al. 2007; Saubin et al. 2016). However, the timescales of bubble nucleation, growth and coalescence within post-fragmentation pyroclastic material remain poorly constrained (Giordano et al., 2005; Ryan et al.,

2015; Clarke et al., 2019). Understanding these systematics is important for understanding porosity and permeability development within shallow conduit magmas at the moment of fragmentation (Giordano et al., 2005; Mueller et al., 2008; Ryan et al., 2015; Clarke et al., 2019). At Chaitén, clast textures record repeated welding and re-opening of a conduit plug, partly overprinted by late-stage vesiculation (Castro et al. 2012; Saubin et al. 2016).

To illuminate bubble growth dynamics in post-fragmentation volcanic bombs, we use a series of high temperature, atmospheric pressure vesiculation experiments to investigate in-situ bubble nucleation, growth and interactions in natural samples of H_2O-rich rhyolitic glass from the 2008 eruption of Chaitén, Chile. Being the only closely observed eruption of high-silica (75 wt. %) rhyolite, Chaitén provides a unique source of fresh rhyolitic glass for which there are excellent constraints on eruption dynamics (Castro and Dingwell, 2009; Forte and Castro, 2019). Our atmospheric pressure experiments simulate vesiculation processes following explosive fragmentation from a conduit. The aim is to understand the extent of post-ejection bubble growth occurring in pyroclasts. Although previous studies have addressed vesiculation dynamics in H_2O-poor melts (<0.5 wt. % H_2O) (i.e. Bagdassarov et al., 1996), we have investigated more water-rich melt (~1 wt. % H_2O) that is typical of bombs ejected in explosive rhyolitic eruptions (Forte and Castro, 2019). Such bombs preserve volatile contents and textures indicative of upper conduit plug formation, partially overprinted by post-fragmentation vesiculation (Saubin et al. 2016).

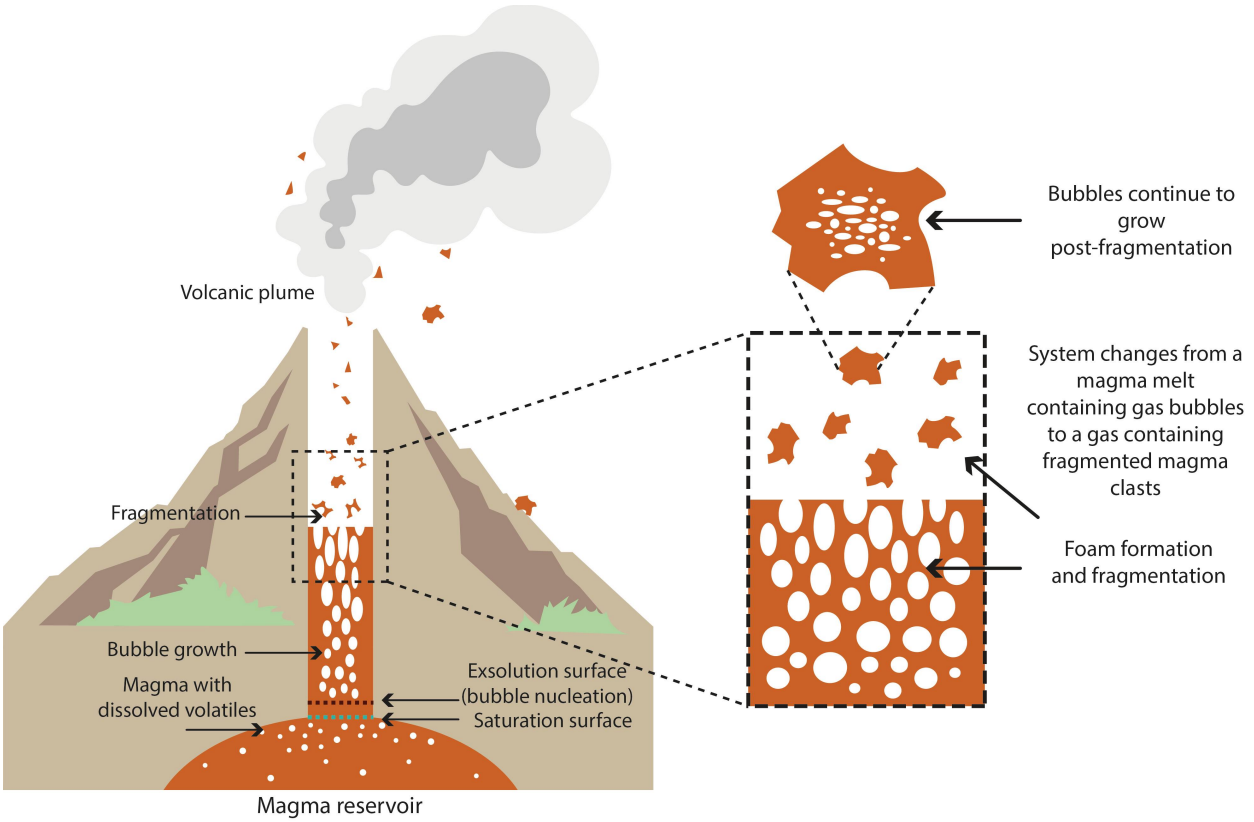

Figure 1. Stages of bubble nucleation and growth leading to magma fragmentation in a volcanic conduit. Individual pyroclasts of pumice may continue to vesiculate past the point of initial fragmentation although this process is dictated by cooling rates within the pumice clast, modified after Gonnermann and Manga (2007).

1.1 Previous experimental bubble growth studies

Several studies involving decompression and heating experiments on silicic melts have sought to gain an understanding of the effects of magma ascent and decompression on bubble nucleation and growth (e.g. Gardner et al. 2000, Hamada et al. 2010, Lavallée et al. 2015; Ryan et al. 2015; Forte and Castro, 2019). Whilst the vast majority of previous bubble growth experiments utilised a heat (and/or decompression) and quench technique whereby the end-member product of vesiculation was recorded in terms of vesicle size distributions (e.g Gardner et al, 1999; 2000; Lui

and Zhang, 2000; Hamada et al., 2010); continuous measurements of in-situ bubble growth are rare (Baker et al., 2012; Masotta et al., 2014; Polacci et al., 2018). End-member analysis of experimentally treated samples have been used to infer mechanisms of bubble growth and coalescence (Burgisser and Gardner, 2004; Gardner, 2007a; Kennedy et al, 2016), as well as shape ideas concerning the efficiency of crystal surfaces for sites of heterogeneous bubble nucleation (Gardner and Denis, 2004; Gardner, 2007b). Bubble growth experiments can be broadly categorised into those that directly measure in-situ growth (e.g. Bagdassarov et al., 1996; Bai et al., 2008; Baker et al., 2012; Masotta et al., 2014; Ryan et al., 2015) and those that use a heat and quench technique to record final bubble sizes (i.e. Hamada et al., 2010). In addition we can differentiate between experiments that induce bubble growth by keeping pressure constant but alter temperature (e.g. Bagdassarov et al, 1996; Lui and Zhang, 2000; Masotta et al., 2014; and our study) and those that keep temperature constant but alter pressure (e.g. Lyakhovsky et al., 1996). Many of the experiments were conducted on real silicic materials with a range of H_2O contents, so comparisons can also be made through experiments on low and high water content material and those that invoked high (>700 °C) or low (<700 °C) temperatures. In one of the first experimental bubble growth studies, samples of Newberry Rhyolite obsidian with a water content ~0.2 wt.% were heated at 0.1 MPa to temperatures of 800-1100 °C (Murase and McBirney, 1973). It was found that bubbles grew at a sluggish rate of around 1-2 x 10^{-8} cm s^{-1} and nucleated rapidly near the beginning of the experiments but both growth and nucleation were significantly reduced by the end of their 50 minute long experiments. Lui and Zhang (2000) found the rate of observed bubble growth in their experiments on basalt, increased with both temperature and initial H_2O content. Masotta et al., (2014) also directly recorded bubble growth in basaltic, andesitic and rhydacitic magmas during heating experiments and found growth rates ranging from 3.4 x 10^{-6} mm/s to 5.2 x

10^{-7} mm/s. They noted the faster growth rates in the primitive magmas. In a conduit setting, it has been hypothesized that the level or amount of supersaturation significantly affects both the timing and distribution of bubble nucleation on crystal surfaces (e.g. Gardner and Denis, 2004) during non-equilibrium degassing as magma ascends (Gardner et al., 1999; Mangan and Sisson, 2000). Permeability and porosity development through interconnecting bubbles greatly accelerates the rate of gas escape, encouraging equilibrium conditions and efficient degassing (Gardner et al., 1999; Larsen and Gardner, 2000; Okumura et al., 2009; Okumura et al., 2010; Kennedy et al., 2016). More recently, Castro et al. (2012) used decompression experiments and tomographic observations of natural Chaitén obsidian with 0.6-1.0 wt. % H_2O to characterise timescales and mechanisms of bubble coalescence. Forte and Castro (2019) conducted 1 atm vesiculation experiments on variably hydrous Chaitén obsidian, finding melt vesiculation for $H_2O \leq 1$ wt.% but explosive decrepitation at $H_2O > 1.4$ wt.% and T>874 °C. Sample failure occurred as the induced strain rate during rapid vesiculation let to non-relaxed melt deformation and stress accumulation. Bubble nucleation and growth in hydrous rhyolitic pyroclasts at low pressure has been additionally observed experimentally during isobaric foaming experiments using a peralkaline rhyolitic melt from Olkaria, Kenya (Bagdassarov et al., 1996). This rhyolite contained ~0.14 wt.% H_2O and was heated to temperatures between 625-925 °C, with bubble growth recorded using a video camera (Bagdassarov et al., 1996) and considered in terms of volume expansion with an exponent of 2-2.5 in the Avrami equation.

In addition to experimental studies, many increasingly sophisticated numerical models of bubble growth have been developed. Bubble growth in an infinite melt has been shown to follow a parabolic growth law, where bubble size increases with the square root of the diffusion coefficient

× time (Sparks, 1978). Later models additionally treat volatile diffusion to the growing bubble (Proussevitch et al., 1993a), and thermal effects related to the heat of volatile exsolution (Sahagian and Proussevitch, 1996). Subsequent work numerically demonstrated that bubble interactions also affect growth rates (Proussevitch and Sahagian, 1998). These different effects play differing roles during magma evolution. Three stages of bubble growth have been postulated in high viscosity melts (Navon et al., 1998). In the first stage, diffusion into a small bubble is efficient in keeping internal pressure in the bubble close to its initial value, and the viscous resistance of the melt limits growth at this stage. During the second stage, bubble pressure is greater than the surrounding melt and growth is then limited by diffusion. In the final stage, which was independently confirmed by Lyakhovsky et al. (1996), bubble growth is influenced by neighbouring bubbles and all supersaturated water diffuses until a final bubble radius is reached. In silicic bombs with >0.95 wt.% H_2O that are rapidly ejected into the atmosphere, ΔP can exceed 7 MPa, as calculated using the H_2O solubility-pressure relationship at 825°C and 0 wt. % CO_2, given the VolatileCalc programme (Newman and Lowenstern, 2002).

The principle aim of the current paper is to provide an empirically derived bubble growth law from direct experimental observations that can be used to provide 1st order approximations of the time scales of vesiculation in post-fragmented pyroclasts in hydrous rhyolitic magmas.

2. METHODOLOGY

2.1 Sample characterisation

The material used during vesiculation experiments was a 2 cm fragment of dense, high-silica (76 wt.%) rhyolitic obsidian (Chaitén obs 3) ejected in the early explosive stage of the 2008-2009 Chaitén eruption. It was collected from close to the caldera edge in July 2008, from amongst bomb-rich pyroclastic fragments thought to derive from Vulcanian explosions in the transitional phase 2 of the eruption, which began in mid-June 2008 (Castro and Dingwell, 2009; Pallister et al. 2013; Saubin et al. 2016). The Chaitén obsidian was chosen as a suitable material for vesiculation experiments due to the hydrous nature of the melt and the minimal microlite crystal content. Additionally, a partially vesiculated rhyolitic bomb ~1 m in diameter was observed and sampled in January 2014 (BOMB-1). This was located within the Chaitén caldera (42º49´38.62″ S, 72º39´32.51″ W), in pyroclastic deposits emplaced during Vulcanian activity in June 2008 (Saubin et al. 2016).

From the original 2 cm fragment we made much smaller millimetric fragments of the Chaitén obs 3 obsidian sample which were double-polished by hand using sandpaper in order to create wafers with thicknesses ranging from about 125 μm (+/- 5 μm) to 212 μm (+/- 13 μm). Inspection of these wafers with a petrological microscope revealed the presence of fresh glass, bearing <2-5 % of small (<20 μm) biotite and pyroxene microlites, in agreement with other studies of Chaitén rhyolite (Castro and Dingwell, 2009). The resolution of our imaging meant that it was not possible to discern nanolites or speculate on their influence (Hajimirza et al., 2020). A small proportion (<5 %) of vesicles were observed, which were largely elongate, <55 μm in length, and preferentially occur in flow bands hundreds of μm to <1 mm in width. Similarly, wafers were created from the dense margin of BOMB-1, with thickness of 132 +/- 5 μm.

Water concentrations in the Chaitén obs 3 sample were determined using a Thermo Nicolet infra-red spectrometer at the University of Lancaster, with a Continuum Analytical microscope, KBr

196 beamsplitter, and a MCT-A detector. Four maps were produced to test for H_2O heterogeneity
197 within the wafer, comprising 162 analyses in total. 128 spectra were collected across wavenumbers
198 of 6000 to 1000 cm^{-1}, at a resolution of 4 cm^{-1}. Raw spectra were processed using an 18-point
199 linear baseline correction that allowed the 5230 cm^{-1} (H_2O_m), 4520 cm^{-1} (OH^-), 3550 cm^{-1} (H_2O_t),
200 2350 cm^{-1} (CO_2) and 1630 cm^{-1} (H_2O_m) peak heights to be discerned. Spectra that showed
201 additional peaks were dismissed, being affected by partial analysis of a mineral phase. No
202 discernible CO_2 was detected, in common with other studies of Chaitén obsidian (Castro and
203 Dingwell 2009; Castro et al. 2012), indicating concentrations less than the detection limits of ~30
204 ppm. Water content (C) was calculated using the Beer-Lambert Law:
205
206 $$C_i = \frac{M_i Abs}{d\rho\varepsilon} \qquad (1),$$
207
208 where *i* refers to the volatile species of interest, *M* is the molecular weight of substance *i* (18.02 g
209 mol^{-1} for H_2O), *Abs* is absorbance (measured peak height), *d* is sample thickness, ρ is glass density
210 and ε is the absorption coefficient. Absorption coefficients of 1.42 l mol^{-1} cm^{-1} (Okumura and
211 Nakashima, 2005), 80 l mol^{-1} cm^{-1} (Leschik et al., 2004) and 55 l mol^{-1} cm^{-1} (Newman et al., 1986)
212 were used for the 4520 cm^{-1}, 3550 cm^{-1} and 1630 cm^{-1} peaks respectively. A glass density of 2275
213 g l^{-1} was used, in accordance with density measurements for similar Chaitén obsidian (Saubin et
214 al. 2016). Maps were re-run in reflectance mode to determine wafer thickness, with reflectance
215 spectra displaying inference fringes collected between 2050 and 2310 cm^{-1}, and wafer thickness
216 given by
217 $$d = \frac{m}{2n(v_1 - v_2)} \qquad (2),$$
218

(von Aulock et al., 2014), where m is the number of fringes that occur between two selected wavenumbers; v_1 and v_2 (in cm^{-1}) and n is the refractive index; 1.5 for rhyolite (Hodder, 1978). A unique sample thickness was thus acquired for every transmission point. The absolute error in water concentration determined by infra-red spectroscopy is approximately 10% (e.g. Dixon et al., 2002; von Aulock et al. 2014; Saubin et al. 2016). The mean measured total H_2O concentration in the wafer was 0.95 wt. %, with <0.1 wt.% variation. Domains of slightly higher H_2O generally coincided with bubble-rich flow bands. All analyses have low H_2O_m/H_2O_t ratios that are indicative of high-temperature magmatic speciation followed by rapid quenching, with negligible post-eruptive hydration (e.g. Owen et al., 2012). Water concentrations in the BOMB-1 obsidian were determined at beam B22 of the Diamond Light Source, Harwell, UK, using analytical techniques described in von Aulock et al., (2014) and Saubin et al. (2016). An aperture of 10 x 10 μm was used, and 174 points were collected at a spacing of 10 μm along a traverse 1.73 mm in length. It was not possible to measure water concentrations in the vesiculated samples after they had been heated, owing primarily to the prohibitively thin glass septa between vesicles. The physical nature of such samples precludes both sample preparation and achievement of good FTIR signal (von Aulock et al., 2014).

2.2 Hot stage and analytical techniques

A Linkam TS1500 hot-stage connected to a Zeiss AxioScope A1 microscope was used as the apparatus for heating experiments (Fig. 2). Temperature calibration experiments conducted by Applegarth et al. (2013), using the known melting points of several metal standards, suggest that recorded temperatures match those of the actual temperature in the sample to within ±2 °C, over the range 157 °C to 1064 °C. A sample wafer was placed onto a sapphire slide where light passes

243 through a 0.8 mm diameter basal aperture and time-lapse images were captured with a digital
244 camera connected to a PC, at a rate of one image every two seconds. Image resolution was
245 determined with a micrometer and gave a pixel size of 0.6 μm (20× objective lens).
246 All of the samples were heated at the same rate (200 °C min^{-1}) to isothermal temperatures spanning
247 575–875 °C, at which they were held for between 8 minutes and 48 hours, with longest dwell times
248 for the lowest isothermal temperatures (Supporting information table 2). The different durations
249 of the experiments represent the time available until bubble growth ceased. These temperatures
250 were chosen to range from below the glass transition temperature *Tg* (~600°C) and to above the
251 inferred eruptive temperature of 825 °C (Castro and Dingwell, 2009). After the isothermal phase,
252 samples were quenched to room temperature (>200 °C min^{-1} cooling above 400 °C). To assess
253 whether there would be any significant lag between the temperature of the furnace and the rhyolite
254 wafers we consider a simple model for conductive heat transfer, in which the thermal diffusion
255 time of a particle with diffusivity *K* and thickness *d* is given by

256 $$\tau = \frac{d^2}{4K} \qquad (3)$$

257 (e.g. Turcotte and Schubert, 1982). In our case, *d* is the water thickness (125-212 μm) and *K* the
258 thermal diffusivity of rhyolite (~5.4×10^{-7} m^2s^{-1}; Romine et al., 2012). The maximum thermal
259 diffusion time, which approximates that of thermal equilibration, is therefore 0.02 s, which
260 corresponds to a lag of 0.07 °C at the maximum applied heating rate of 200 °C/min. This is
261 negligible compared to the uncertainty of furnace temperature (±2 °C), and thus we can assume
262 that the wafers effectively retained thermal equilibrium throughout all experiments.
263

During experiments, care was taken to ensure growing vesicles remained in focus; however non-uniform vesicle growth drove variable expansion within the field of view, compromising the ability to capture fully-focused images.

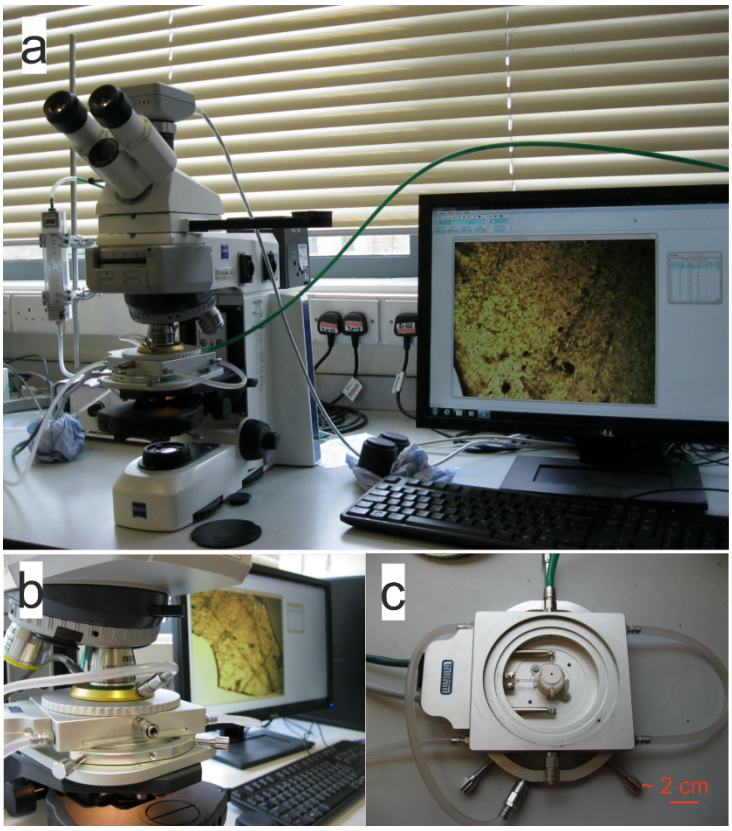

Figure 2. Hot-stage microscope setup. Sample is placed inside a ceramic furnace (c), temperature is set by a Linkam TS1500 heated stage mounted on a Zeiss Axioscope (b). In-situ observations are made on a connected PC (a).

2.3 Bubble growth measurements

To calculate bubble growth rates, individual bubbles were tracked with a time-lapse image sequence using 'Pointcatcher' (http://tinyurl/pointcatcher), a Matlab-based time-lapse analysis

278 software (James and Robson, 2014). The code enables bubble growth to be measured by tracking
279 individual points, manually identified on the bubble perimeter and measuring the distance between
280 points. Bubbles were chosen for measurement based upon the quality of focus in individual
281 frames, and the initial distance from other bubbles or the sample edge. Ideal bubbles with which
282 to obtain growth rates were those with sufficient space (many tens of microns) for free growth
283 before the onset of inter-bubble interactions in an expanding foam. All of the measurements are
284 two-dimensional and we could not account for growth in the 3rd dimension, into the sample.
285 However, since the sample diameter is approximately 1000 times the sample thickness we assume
286 that the growth and dynamics observed in the dimension and field of view is representative. We
287 monitored the growth of 14 bubbles in the tests at 725°C, 16 bubbles at 775°C, 22 bubbles at
288 825°C, and 23 bubbles at 875°C, which we used to determine the growth rates for each different
289 test. Each individual bubble was marked, manually, with four separate points, two corresponding
290 to the maximum diameter (b-axis) and the other two for the minimum diameter (a-axis). In the
291 vesiculation experiments bubbles are identified as black patches within a yellow (false colour)
292 melt (Figure 2). Measurements were made on the edge of bubbles where there was a clear contact
293 between bubble and melt. However, at the edge of these dark patches the melt-bubble boundary
294 can be unclear. The accuracy of measurements is dictated largely by image focus, it is noted that
295 changes in focus can contribute to an additional +/- 5 μm uncertainty in bubble edge locations,
296 estimated at room temperature defocussing. The smallest bubbles measured had a diameter of 8
297 μm (+/- 5 μm), and the largest a diameter of 202 μm (+/- 10 μm). The bubble-melt boundary is
298 defined by a clear colour contrast; however, the contrast between bubble-bubble boundaries is
299 much less clear. Quantitative bubble measurements are made up until the a and b diameters can no
300 longer be discerned due to interaction with neighbouring bubbles (Fig. 4). Uncertainty with respect

to user measurement error (σ_d) was reduced by conducting three repeat measurements on each bubble in a single original image (measurement uncertainties were of order +/-5 μm). The error with respect to growth rates was calculated from the measurement uncertainty through error propagation. Minimum and maximum bubble diameters (d_a and d_b respectively) are used to calculate aspect ratios (AR) to assess bubble shape evolution and relationship with growth rate,

$$AR = \frac{d_b}{d_a} \quad (4)$$

The uncertainty in aspect ratio, σ_{AR}, is dictated largely by measurement error,

$$\frac{\sigma_{AR}}{AR} = \frac{\sigma_a}{d_a} + \frac{\sigma_b}{d_b} \quad (5)$$

Where σ_a and σ_b are the standard deviation about the mean of length measurements along the a and b axes of each bubble. Equation 7 has the condition that $\sigma_a \ll d_a$ and $\sigma_b \ll d_b$, which is fulfilled because, although the smallest measured bubbles are ~10 μm and the maximum measurement error on these bubbles is ~5 μm, the largest bubbles (>50 μm) have larger measurement errors, particularly when neighbouring bubble walls touch (e.g. at least +/-10 μm). This error results from defocussing as samples expand and the effects of neighbouring bubble walls where the error on measurements is difficult to quantify but at least +/- 10 μm.

The growth-temperature relationship was determined using the average growth rate ($\bar{v}_r$) of different bubbles at each temperature within the elapsed period of isothermal free bubble growth. Average growth rates were obtained by

$$\bar{v}_r = \frac{d_f - d_i}{t_f - t_i} \quad (6)$$

where subscript *f* denotes the final and *i* the initial values within the section of free growth as previously described, *d* is bubble diameter in either the a or b axis and *t* is time. The calculation considers two dimensional bubble growth rather than volumetric changes. Error in growth rate (σ_{Vr}) was calculated based upon the maximum measurement error (σ_d) where

$$\sigma_{vr} = \left(\frac{1}{t_2 - t_1}\right)(\sigma_{d_2} + \sigma_{d_1}) \qquad (7)$$

Maximum growth rate error of +/- 0.18 μm s^{-1} was calculated in the highest temperature experiments but reduced to <0.05 μm s^{-1} in lower temperature experiments. This growth rate error is smaller in lower temperature experiments because bubble sizes were generally smaller and there were less bubble interactions.

2.4 Magma viscosity and melt diffusivity

Magma viscosity for each temperature tested was calculated using the method of Giordano et al (2008), based upon the composition of Chaitén rhyolite (from Castro and Dingwell 2009), the measured H_2O concentration of our sample, with 0 ppm CO_2. CO_2 was not detected in our samples and is therefore not incorporated into the viscosity calculations. The effect of crystals on effective viscosity (η) was estimated using the Einstein-Roscoe equation (Einstein, 1911; Roscoe, 1952; 1953)

$$\eta = \eta_o(1 - \phi C)^{-2.5} \qquad (8),$$

where η_o is the viscosity of crystal free melt, ϕ is a constant (1.67) and *C* is the volume fraction of suspended crystals. Due to the low crystal content of analysed samples, the effect of crystals on viscosity is negligible: the addition of 10% crystals at 875°C raises the magma viscosity from

343 $10^{7.05}$ to $10^{7.24}$ Pa s. None of the experiments induced noticeable crystallization and therefore the

344 crystal fraction remained constantly low.

345

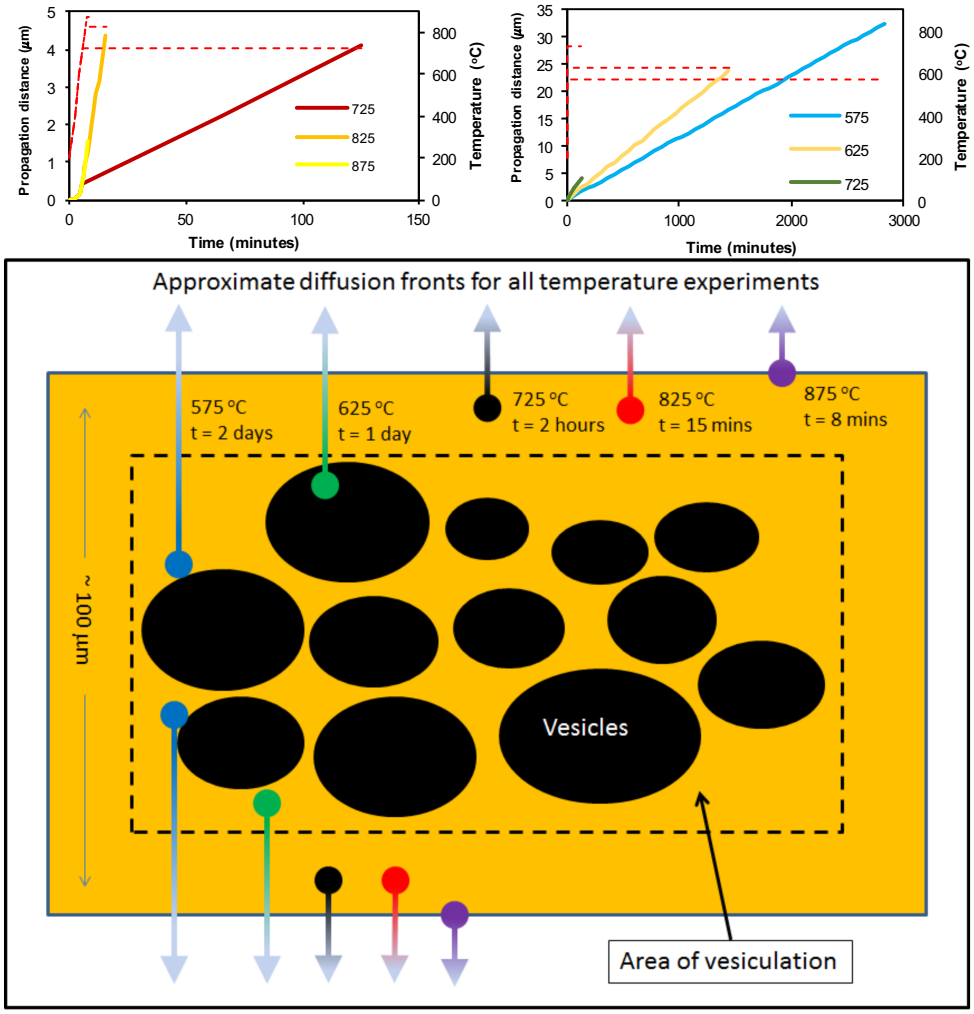

346

347 *Figure 3. Diffusional front propagation as a function of time and temperature (above), where*

348 *dashed lines represent the imposed temperature and solid lines are the modelled diffusion*

349 *distance. Below, a schematic diagram of a cross section through a ~100 μm thick vesicular*

350 *obsidian wafer showing the approximate distances that the diffusional front propagated into the*

351 *sample. Maximum diffusion propagation is 32 μm over a period of ~ 2 days held at 575 °C (top).*

352 *In contrast the diffusional front for the highest temperature experiment (875 °C) only propagated*

353 *1.5 μm into the sample; however this occurred over a much faster timescale (~ 8 minutes).*

354

One of the complexities of the atmospheric pressure hot-stage method is diffusive loss of H_2O from the sample surfaces. Thus, even without vesiculation, sample water content will vary through time and space throughout an experiment, potentially influencing estimates of the viscosity and H_2O content of vesiculating melt. This could be particularly important in longer-duration experiments. As we were not able to directly measure the water concentration of samples after the heating experiments a model based on Zhang (1999) was used to estimate the timescale of diffusive dehydration (D_{H2Ot}) where C_o and C are water concentration inside and outside of the sample respectively

$$D_{H_2O_t} = \left(\frac{C}{C_o}\right) exp\left(-16.83 - \frac{10992}{T}\right) \quad (9)$$

where C = 0.95 wt.% and C_o = 1 wt.%. The model used calculates $\sqrt{(D_{H_2O}t)}$ and provides an approximate distance that the diffusion dehydration front will propagate into the sample over time (Fig. 3), where T is temperature. It is found that diffusional degassing is unlikely to have significantly affected measured growth rates in most of the experiments, where diffusion fronts only propagate ~5 μm into the edge of wafers (Fig. 3). Due to the long duration of the lowest temperature (575-725˚C) experiments, diffusive H_2O loss likely affected the distribution of water in these samples. Our model suggests that diffusional fronts propagated up to 30 μm into the sample in these low temperature experiments. In all experiments, including those that attained high final vesicularity, the sample surface displayed a continuous "skin" of dense, unvesiculated melt ~microns in thickness, as observed outgassing experiments on rhyolitic obsidian (von Aulock et al., 2017). This reflects how such diffusive degassing at the wafer surface can stifle bubble nucleation (Saubin et al. 2016) and create an impermeable barrier that can prevent foam collapse

(von Aulock et al., 2017). Most of the tracked bubbles grew near the interior of the sample at >> 5 μm from the upper sample surface.

3. RESULTS

3.1 Nucleation, growth and evolution of vesicles

All starting glass wafers, which were prepared from the same centimetric obsidian clast, initially contained between ~1 and ~10 % of vesicles ranging in size from 8–55 μm, estimated from manually picked pixel percentages in optical images. Those vesicles were randomly distributed, except for clearly-defined banded zones of greater vesicle abundance in some wafers (Supplementary data). Pre-existing vesicles were predominantly elongate with maximum aspect ratios of 2:1, where the *b*-axes were commonly near-parallel to flow banding as defined by bands of enhanced bubble and microlite content. Short inter-bubble wall distances within bubble-rich bands permitted only a brief period of uninhibited growth during heating experiments, prior to bubble-bubble interactions (Fig. 4). The interactions can be, at least, partly discerned from the curves of growth with time, where the two highest temperature tests display sigmoidal curves, indicating an initial period of slow growth rate, followed by an acceleration and near-linear growth rate (as used to calculate the averaged growth rates used in the later analysis) and a final reduction in growth rate after the isotherm was reached (Fig. 5). At the lowest temperature test we note a decaying growth rate long after the isotherm was reached. In the highest temperature (875°C) experiments we note five stages of bubble evolution (Fig. 5):

1) Relaxation of pre-existing bubbles;

2) Free growth and nucleation;
3) Nearest neighbour interaction;
4) Coalescence and
5) Foam formation.

The initial stage of bubble growth involved the relaxation of elongate vesicles into spheres. Initial growth rate of the *a*-axis was therefore often faster than the corresponding rate for the measured *b*-axis (Fig. 5). Initial bubble growth occurred during the heating phase (i.e. under non-isothermal conditions) in those tests where the sample was held at temperatures greater than ~750 °C (Fig. 4), however the vast proportion of bubble diameter change during this phase was related to bubble relaxation. Once bubbles had relaxed into spheres with aspect ratios of ~1, we then note a period of free bubble growth as opposed to re-rounding. We also note the first appearance of new bubbles in stage 2 during isothermal conditions, indicating bubble nucleation.

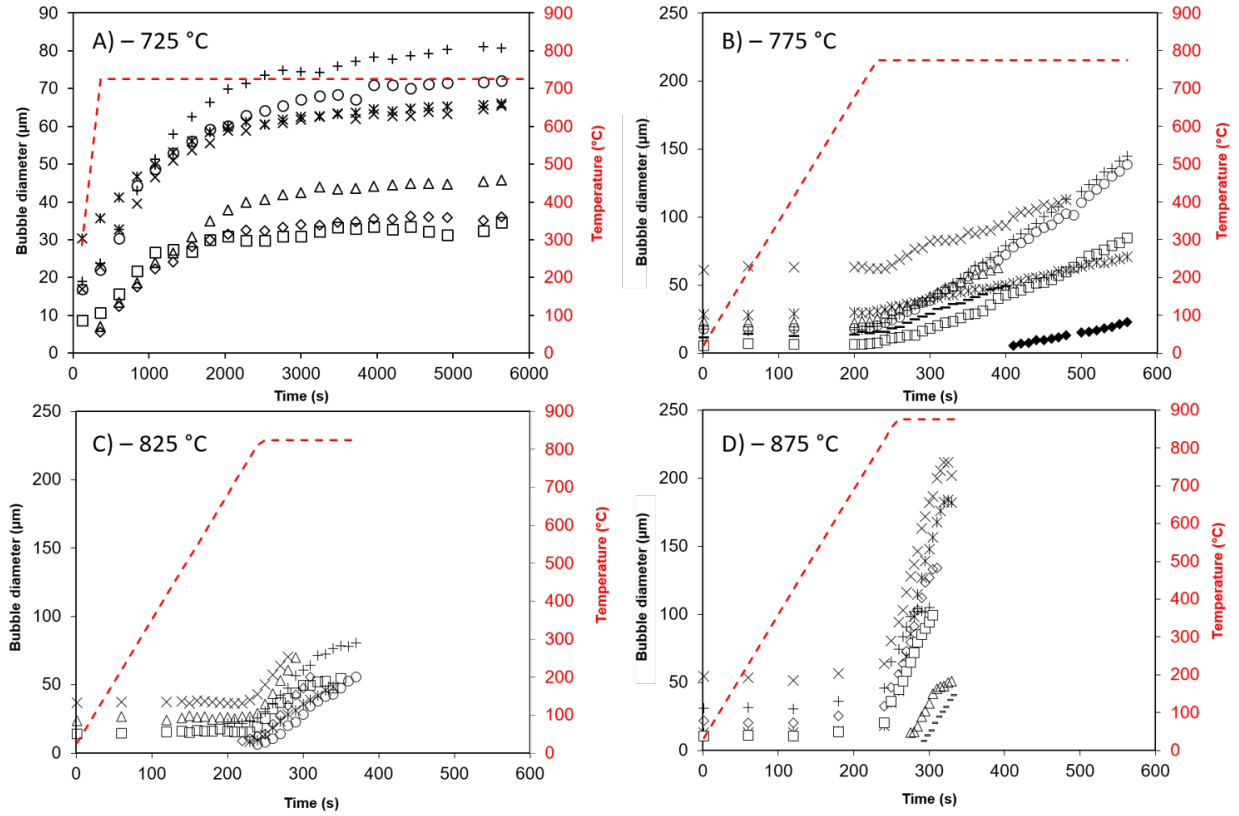

414

415 *Figure 4. Bubble diameter against time for various maximum hold temperatures, A) 725 °C, B)*
416 *775 °C, C) 825 °C and D) 875 °C. Note that the bubble diameter axes and time are different from*
417 *the other plots in section A. This is because the duration of the experiments was one order of*
418 *magnitude longer than the others. The different symbols represent the measurement of individual*
419 *bubbles. The dashed red line indicates the temperature. For clarity, not all of the measured*
420 *bubbles are shown.*

421

422 As bubbles continued to grow they began to interact with their neighbours, resulting in flattening
423 of adjacent bubble walls, with the flattened surfaces normal to a line joining the two bubble centres.
424 From the onset of bubble wall flattening, growth parallel to this bubble centre-centre line slowed
425 significantly, sometimes resulting in a decreased bubble diameter in this orientation. However, in
426 these cases, enhanced growth was instead observed along an axis normal to the centre-centre-line
427 and parallel to the flattened surfaces, providing growth was not impinged by nearby bubbles in

that direction (Fig. 6). Through this process, bubbles became highly elongate and non-spherical. Bubble wall flattening was noted even when adjacent bubble walls were not in direct contact, often with a melt gap of ≤30 μm separating neighbouring bubbles. Unlike previous coalescence experiments on hydrous rhyolitic melts (Castro et al. 2012), no dimpling of bubble walls was observed – a phenomenon attributed to inter-bubble pressure differentials. Therefore in our experiments the vapour pressure in adjacent bubbles appears to have been similar. The final two stages of foam formation and bubble coalescence were only noted in the highest temperature experiments (Supplementary data). We define a foam here to simply mean a state when a majority of the bubbles were interconnected, with bubble to melt ratios ≥ 3:2. We note that this is slighty different to the definition of Proussevitch et al., (1993a) who define a foam as >74% vesicularity. This is simply because at bubble to melt ratios of 3:2 it was not possible to accurately constrain vesicularities as the samples changed shape substantially, influencing the range of focus, as previously discussed. Bubble coalescence occurred in some experiments (Fig. 5), as inferred predominantly from bubble number densities rather than direct observations. During foam formation and multiple bubble-bubble interactions promoted highly-deformed, non-spherical bubble shapes. Two bubble size populations are observed qualitatively during the foaming process, with small bubbles (<8 μm) continuing to nucleate and grow within thin melt pockets separating larger bubbles. It was not possible to discern, with confidence, the mechanism of nucleation, whether on crystal surfaces or not although we speculate the nucleation was heterogeneous due to the presence of microlites within the melt. Further analysis of the kinetics of bubble nucleation were limited by resolution and imaging technique which only permits imaging of features >1 μm in dimension. Several samples included microlite-rich bands that commonly contained an initial higher bubble number density, as well as being slightly more H_2O-rich, suggesting that

heterogeneous nucleation had occurred during disequilibrium degassing prior to quenching during explosive ejection. During stages 4 and 5, small newly-formed bubbles commonly coalesced with older and larger bubbles, apparently via stretching and thinning of inter-bubble melt walls. Smaller bubbles generally grew slower than the larger bubbles in whose walls they were growing. Foam formation was observed at isothermal temperatures of ≥775 °C, whereas below this temperature insufficient bubble growth and coalescence occurred to create foam textures.

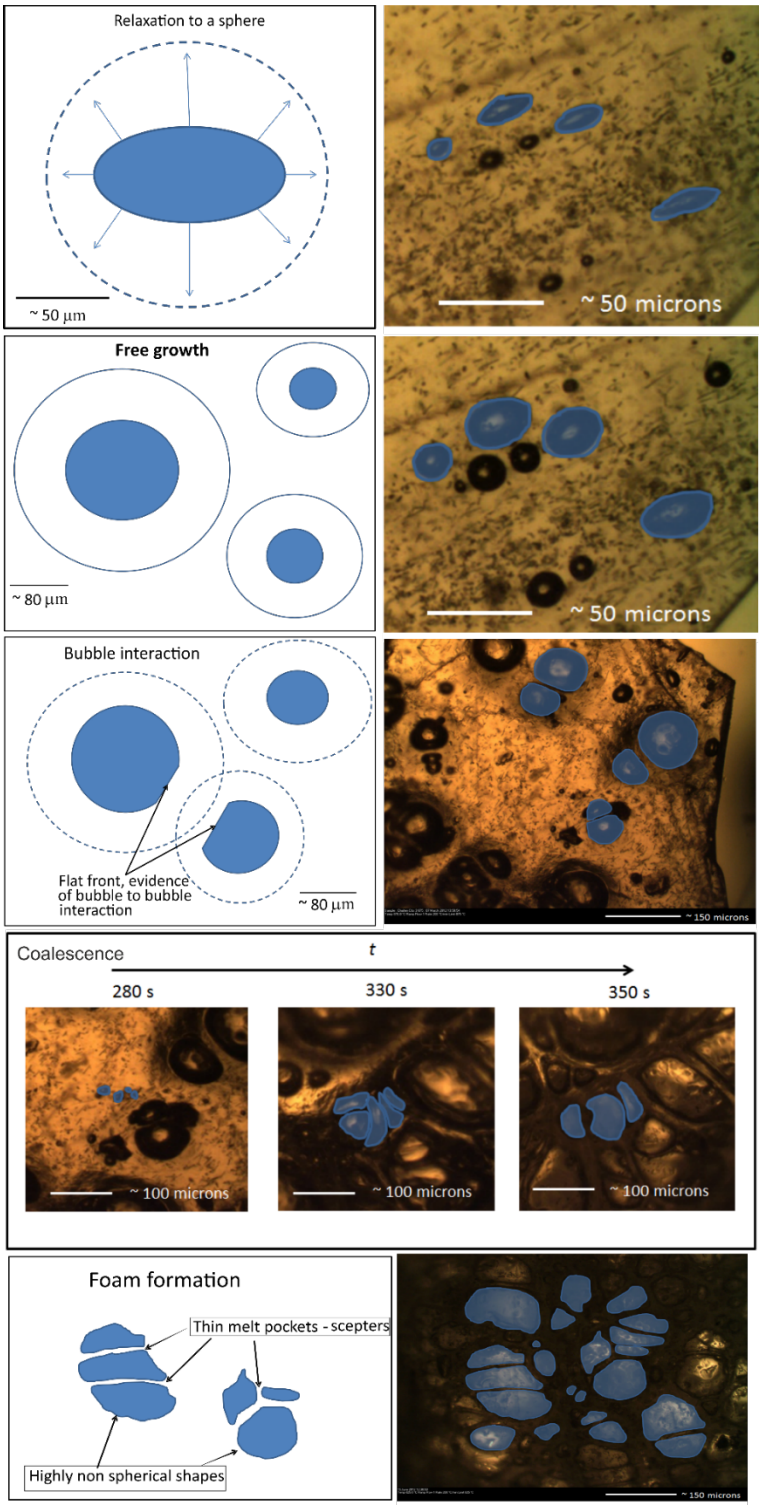

458

459 *Figure 5. Five stages of bubble growth 1) Relaxation of pre-existing bubbles, 2) free growth*
460 *and nucleation, 3) nearest neighbour interaction, 4) coalescence and 5) foam formation.*

461

3.2 Temperature-dependent bubble growth rate

The growth of individual bubbles was tracked during the heating phase and over a range of isothermal temperatures during a hold phase. In Figure 4, we show the growth of individual bubbles over four of the temperatures investigated. The early stages of heating show no bubble growth below approximately 725 °C in all tests. Above this temperature all bubbles exhibit a period of near-constant growth rate, during both heating (non-isothermal) and isothermal conditions. Whilst full modelling of the growth trajectories would be possible we have chosen to derive the average growth rates for each temperature considering this period of free growth as the growth with time is linear in this portion. We found that in the highest temperature tests (at 875 °C) where ΔT (between initial bubble growth temperature and hold temperature) was approximately 150 °C, bubble growth rates ranged from between ~0.32 μm s^{-1}, as the sample reached 725 °C, and up to ~1.27 μm s^{-1}, as the sample reached the desired hold temperature of 875 °C. This large difference of growth rates reflected the range of temperatures through which the sample experienced on the way to attaining the desired hold temperature. As such for later comparison we deal only with the averaged growth rates obtained during both the period of free growth but at isothermal conditions, when the hold temperature was attained. It is important to note that the growth rates obtained under non-isothermal conditions do correspond well with the averaged growth rates obtained during each hold phase in the lower temperature tests. In these lower temperature tests bubble growth is only observed when the hold temperature is reached, and this is why for comparison between tests we deal only with growth during these maximum hold temperatures. To clarify, all growth rates discussed from here on relate to bubble growth during the isothermal phase of our tests, where bubble growth was near constant. Near-constant growth

rate began when a bubble reached ≥ 5 % of its initial size regardless of whether growth occurred isothermally or non-isothermally. The aspect ratio of bubbles is rarely constant, therefore for the purpose of obtaining growth rates (i.e. measuring growth rather than relaxation), only measurements obtained within measurement error of an aspect ratio of 1 were used. This growth phase occured only after the attainment of maximum temperature in all tests. The time interval of constant growth, which ranges from ~30 seconds at 875 °C to ~30 minutes at 725 °C is dictated largely by the initial bubble number density (BND) (Supplementary data), whereby higher BNDs increase the likelihood of bubble-bubble interactions and reduce the time interval available for the measurement of constant growth. For example, we performed repeat tests at 825°C as one of the samples contained approximately 300 bubbles mm^{-3} and the other contained approximately 3000 bubbles mm^{-3} . This hence influenced the chance of bubble-bubble interactions but it did not substantially change the average growth rates derived (Supporting information).

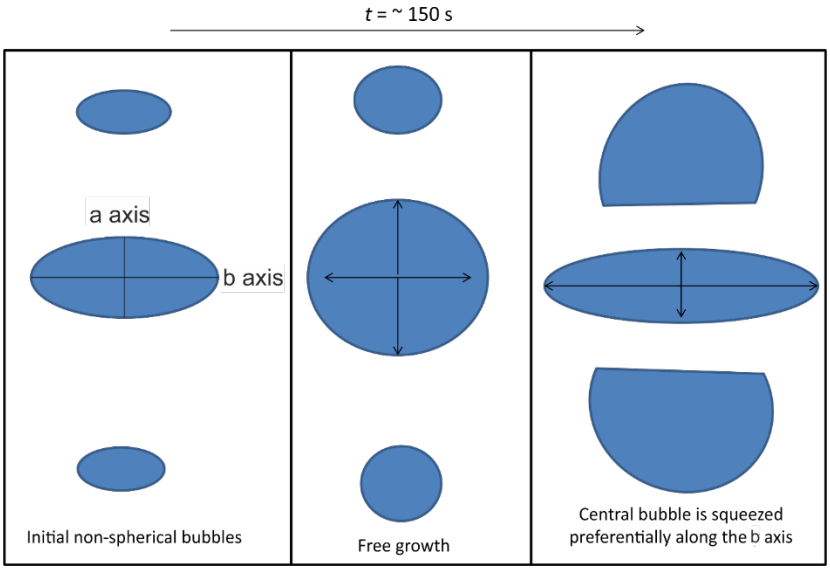

Figure 6. Effect of bubble deformation on observed growth rate. Here the measured b-axis of a bubble appears to grow faster but this effect is due to neighbouring bubbles preferentially squeezing the measured bubble along the b-axis. The reverse situation is also observed, whereby slower than expected growth is found on the b-axis.

No bubble growth was observed in experiments at temperatures < 725 °C. At 725 °C, a maximum of 9 μm of growth along the *a*-axis occurred over a period of ~30 minutes, indicating a sluggish growth rate of ~0.5 × 10^{-3} μm s^{-1}. No growth was observed after this time or at all along the *b*-axis. The growth was minimal and characterized by relaxation of pre-existing vesicles towards a more spherical form, with expansion of their *a*-axis only, and so is better defined as shape relaxation rather than true growth. Far higher growth rates were determined for higher-temperature experiments, reaching 1.27 μm s^{-1} at 875 °C, and the bubble growth rate as a function of viscosity (Fig. 7a) and temperature (Fig. 7b) describes an exponential relationship where $V_r = 3270.26e^{-1.117\eta}$ and $V_r = 5.57\times10^{-7}e^{0.016T}$ respectively. The best fits were simply the most appropriate empirical choice of simple functions to provide a relatively easy tool for later interpretation and modelling. The duration of growth over which the bubble growth rates were obtained account for only a small portion of the total test duration of our vesiculation experiments, as shown in Figure 4. However, it was only in this period that we could be confident that the bubble growth was not impacted by morphological interactions between bubbles.

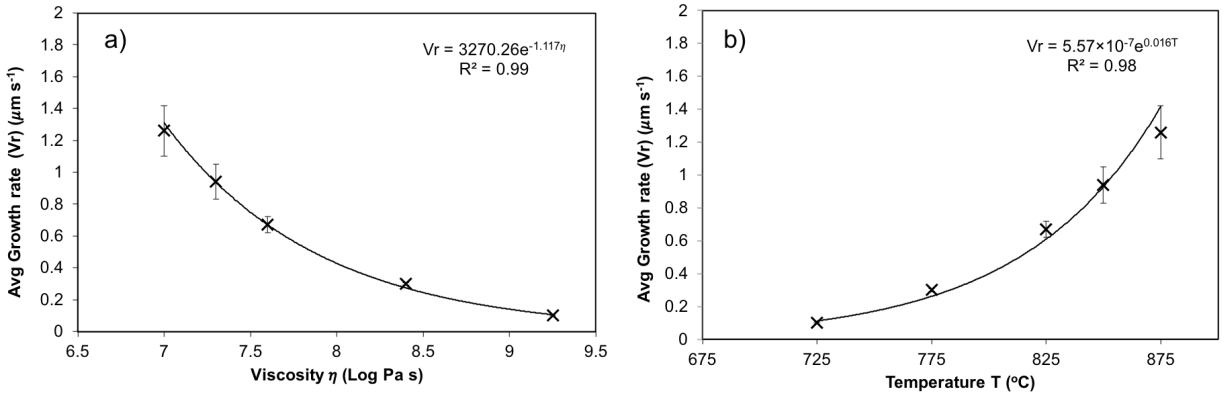

Figure 7. a) Exponential relationship between experimentally derived averaged bubble growth rates and modelled melt viscosity (from Giordano et al., 2008) and b), averaged bubble growth rates and temperature.

4. DISCUSSION

Our isothermal bubble growth results are now considered in the context of an ejected cooling bomb model. The aim is to investigate the maximum attainable bubble size in clasts of rhyolite ejected during Vulcanian explosions. It must be reiterated that the experiments were conducted under atmospheric conditions, without the application of external stress (Hajimirza et al., 2019) or confinement and hence are most relevant to conditions occurring outside of the volcanic conduit such as in ejected large volcanic bombs.

4.1 Observing the physical processes of vesiculation

The results presented here provide direct observations of bubble growth in a rhyolitic melt. Most of our samples contained some pre-existing elongated vesicles, often aligned in bands. The existence of non-spherical bubbles indicates that the timescale of natural pyroclast cooling was faster than that of viscous bubble relaxation. The relaxation timescale can be estimated by $\tau_{rel} = R\eta / \sigma$ (Navon et al., 1998), where σ is the surface tension of a bubble, estimated at ~ 0.106 N m^{-1} (Mourtada-Bonnefei and Laporte, 2004). Taking the estimated melt viscosity of $10^{7.1}$ Pa s at 875 °C (from Giordano et al. 2008), an initially elongate 10 μm bubble should relax within 20 minutes. This far exceeds the short relaxation timescales observed in our higher temperature experiments (~5 s). Changing values of surface tension within an order of magnitude does not significantly change the estimated relaxation time and it is unlikely that an order of magnitude difference in surface tension would be experienced here. The disparity between the findings here and the

545 modelled outcome must instead be due to an overestimate of the viscosity, for example a change
546 in viscosity to 10^6 Pa s corresponds to a relaxation time of ~ 2 seconds, which is in far better
547 agreement with our observations. Such dramatic viscosity changes can be achieved by temperature
548 increase or the addition of H_2O (Giordano et al., 2008). In our strain-free experimental procedure
549 localised strong temperature increase is implausible, leaving locally high H_2O at bubble walls as
550 the only possible explanation. Strong H_2O enrichment around large (millimetric) bubbles in
551 rhyolitic pyroclastic obsidian has been identified (Watkins et al. 2012), and also found in
552 experimentally decompressed samples (McIntosh et al., 2014). Enrichment, attributed to either gas
553 pressure increase or H_2O resorption during cooling, occurs within 20-1000 microns of bubbles,
554 and can involve local H_2O increase of up to 2 wt % above the "far-field" concentration (McIntosh
555 et al., 2014). It is possible that similar enrichment occurs around pre-existing bubbles in Chaitén
556 obs 3 sample, but the small bubble size and large aperture associated with benchtop FTIR analysis
557 precluded quantification of any heterogeneities. The relaxation stage of growth is followed by a
558 free growth stage, whereby spherical bubbles continue to grow without visibly interacting with
559 neighbouring bubbles. The timescale of this growth phase is limited by initial bubble number
560 density where more bubbles decrease the space available for free growth.
561
562 Bubble growth rate decreases exponentially with increasing viscosity. At the highest temperatures
563 (875 °C) diffusivity (Eq. 10) is estimated to be ~ 2.3×10^{-13} m^2s^{-1}, and at the lowest temperature
564 (575 °C) ~3.5×10^{-15} m^2s^{-1}. This relationship suggests that bubble growth rate varies linearly with
565 diffusivity, with diffusivity increasing exponentially with temperature (Supplementary
566 information).
567

Bubble interaction is an important influence on the growth rate in our experiments, and thus is the defining feature of the third stage of bubble growth. This finding is in disagreement with that of Lui and Zhang (2000), who found that bubbles do not significantly affect the growth rate of their neighbours. In contrast, our measured growth rates are significantly impacted as bubbles interact (see also Proussevitch et al., 1993b). As discussed, all of the measurements consider only a two-dimensional field but it is possible that some of the growth or interaction is accommodated in the third dimension, which we could not image accurately. However, whilst we cannot discount this possibility, we expect the effects will be less since the samples are approximately 1000 times longer than they are thick. Bubble interactions eventually lead to coalescence and foam formation in the highest-temperature experiments, which is also marked by a decrease in growth rate. The formation of dense bubble packing and foams in magma are significant in creating degassing pathways through interconnected bubbles, and whilst this did not occur in our experiments, can be followed by compaction and foam collapse (Stasiuk et al. 1996; Kennedy et al., 2016; Forte and Castro, 2019), especially if diffusively degassed dense skins are removed (von Aulock et al., 2017). During the foam formation stage it is expected that growth decreases or stops as volatiles have a defined degassing path. At this stage the major limitation of volatile movement is the increasingly high melt viscosity as volatiles escape, and a viscous quench of the melt may be experienced at this point (Proussevitch et al., 1993b; Thomas et al., 1994). Our results broadly agree with those of Thomas et al., (1994) who find that a viscous quench at viscosities $>10^9$ Pa s prohibits bubble growth. In our lowest temperature experiments we estimate viscosities of $10^{9.5}$ Pa s with very minimal growth rates (0.02 μm s^{-1}), which largely relates to bubble relaxation rather than real growth. Although not proven with our FTIR data, localised H_2O enrichment at bubble walls could

590 have locally reduced melt viscosity to $\leq 10^9$ Pa s, thus facilitating the observed low-temperature
591 relaxation.
592
593 4.2 **Relationship with natural bomb textures at Chaitén**
594
595 Our experimental results provide a two-dimensional framework for estimating vesicle growth
596 timescales at atmospheric pressure in moderately water-rich rhyolitic bombs that do not experience
597 external stresses. With the rate of vesicle growth expressed as a function of melt viscosity, we can
598 also approximate vesicle growth rates in bombs over a range of water concentrations – assuming
599 that there is sufficient supersaturation for initial bubble nucleation. The presence of microlites in
600 Chaitén melts will lower the supersaturation threshold, and textural and water content analysis
601 indicates ~4 MPa is sufficient for vesicle nucleation in Chaitén bombs (Saubin et al. 2016). As the
602 H_2O solubility at 4 MPa is ~0.7 wt. % (at 825 °C and CO_2-free), sufficient supersaturation on
603 ejection to atmospheric pressure is therefore assured for bombs with ~0.7 wt. % H_2O and above as
604 determined from the model of (Newman and Lowenstern, 2002). Here we examine the
605 implications of temperature-dependent bubble growth rates for the extent of post-fragmentation
606 vesiculation in ejected bombs. We consider the conductive cooling of an initially-dense bomb of
607 1 m in diameter, which is instantaneously ejected from the vent at the initial eruptive temperature
608 of 825 °C. Conductive cooling of a spherical body (Carslaw and Jaeger, 1959) can be approximated
609 by:
610

611 $$T = T_o - \left(\frac{2}{\pi}\right)\left(\frac{a}{r}\right)\left(T_1 - T_0\right)\sum_{n=1}^{n=\infty}\frac{(-1)^n}{n}\sin\left(\frac{n\pi r}{a}\right)\exp\left(\frac{-kn^2\pi^2 t}{a^2}\right) \qquad (10),$$

where k and a are the thermal diffusivity and radius of the body respectively, T is the temperature at a distance r from the centre of the body at a time t, T_1 is the body's initial temperature and T_0 is the fixed temperature at the surface of the sphere. This provides the temperature as a function of position and time within the cooling bomb. In the model shown in Figure 9 we used a set value of of 7×10^{-7} m^2 s^{-1} for k with an initial temperature T_1 of 825°C. We then consider the extent of vesiculation within the bomb using the derived relationships for bubble growth rate. For melt with an initial water concentration of 0.95 wt. %, as the sample analysed in this study, growth rate $V_r = 5.57 \times 10^{-7} e^{0.016T}$. However, more broadly, the growth can be approximated as a function of viscosity where $V_r = 3270.26 e^{-1.117\eta}$. The latter equation, when combined with a model of melt viscosity as a function of temperature and H_2O concentration, can be used to approximate vesicle growth rates at a range of different water concentrations. We acknowledge that the residual water concentration will decrease during vesicle growth, due to diffusive transfer of H_2O from melt to vapour, as examined in variably-vesiculated Icelandic obsidian (Owen et al., 2013). However, at the low confining pressure within an ejected bomb (1 atm), this decrease is negligible, even when high vesicularity has been reached.

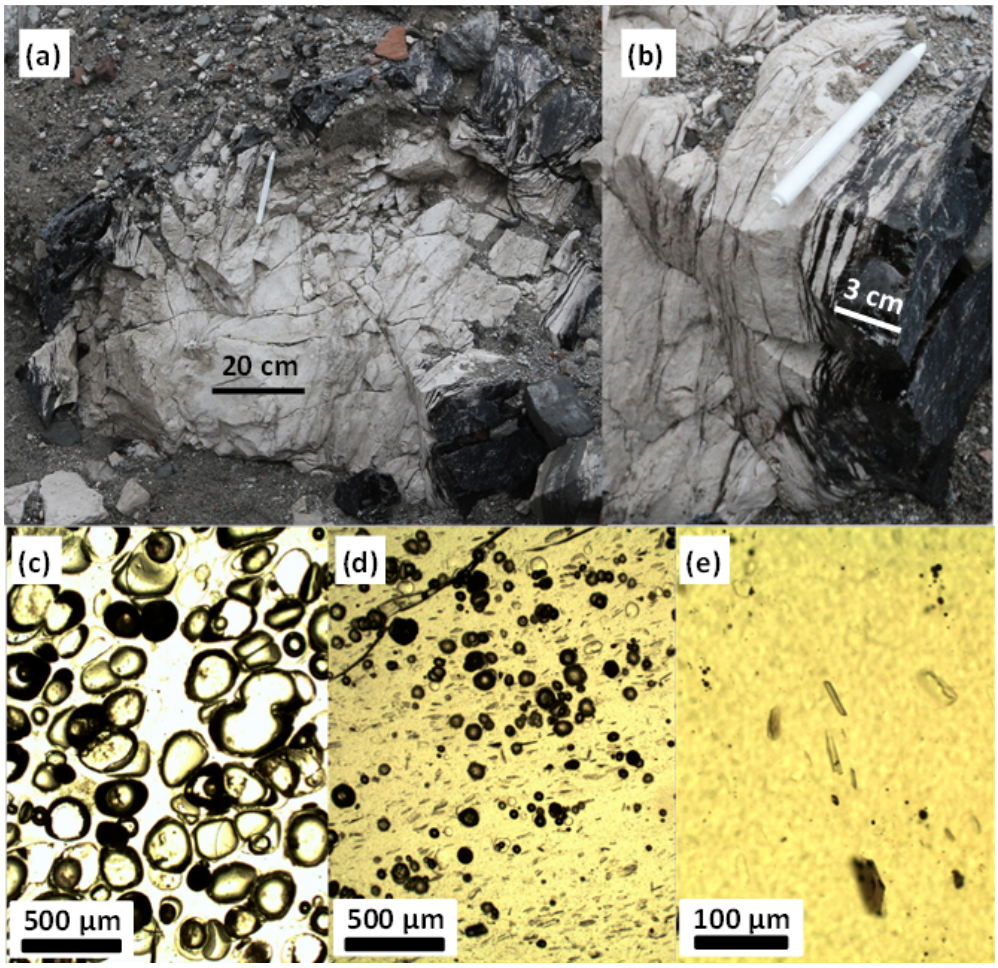

Figure 8. a) Rhyolitic breadcrust bomb from May 2008 Chaitén pyroclastic deposits, at 42°49′38.62″ S, 72°39′32.51″ W, photographed in January 2014. The 1 m-diameter bomb comprises a highly expanded, pumiceous centre (white) enveloped by a dense black obsidian margin that is 3-5 cm thick. The apparently thicker margin top right is of similar true thickness. b) Detail of bottom right-hand portion, where a 3 cm-thick dense outer margin grades into a 2 cm-thick partially-vesicular transitional zone. Patchy vesiculation reflects derivation of the bomb from a welded breccia with variable H_2O concentrations (Saubin et al. 2016), with subtle spatial variations in H_2O concentration persisting. c) Typical textures in the expanded interior, with >60 % highly coalesced bubbles 100-500 µm in diameter. d) Textures in the moderately vesicular transition zone 3-5 cm from the bomb margin, with ~30 % largely isolated bubbles up to 150 µm in diameter. d) The dense quenched marginal material contains a low proportion (<1 %) of spherical bubbles <15 µm in diameter.

642 We thus consider the post-fragmentation vesiculation of BOMB-1, a 1 m-diameter partially-
643 vesiculated, near-spherical bomb with a prominent dense margin (Fig. 8). Infra-red spectroscopic
644 results indicate a water concentration of 0.68 wt. % in the 3 cm-thick dense margin, with a standard
645 deviation of 0.01 wt. % and extreme values of 0.64 and 0.72 wt. % (see Supplementary data). The
646 dense margin contains <1 % vesicles <15 μm in diameter (Figure 9e), in great contrast with the
647 highly-inflated bomb centre (Fig. 8c; porosity ~72 %, determined using a bead displacement
648 method on a 2 x 2 cm sample; Halliwell, 2014). The transitional zone ~3-5 cm from the bomb
649 margin displays an intermediate vesicularity (~30 %) with bubbles attaining 150 μm in diameter.
650 We have used a numerical approach to solve for the evolving radii of vesicles at a range of
651 distances from the outer surface of the bomb, accounting for both conductive cooling (Eq. 10) and
652 viscosity-dependent growth rates. Figure 9 shows the modelled evolution of bubble size as a
653 function of distance from the bomb margin. It indicates that insignificant bubble growth will occur
654 in the outer ~2 cm of the bomb with 0.68 wt. % H_2O, with bubble radii only attaining ~10 microns,
655 similar to the measured bubble sizes (Fig. 8e). However, there is scope for significant bubble
656 expansion >5 cm from the bomb surface, with bubbles sizes approaching hundreds of microns,
657 sufficient for bubble-bubble interaction and the formation of foam textures with a high final
658 vesicularity. The thickness of a dense rind on a 1 m-diameter bomb with this water concentration
659 would therefore be expected to lie between 2-5 cm. This estimate agrees well with the measured
660 dense rind thickness on BOMB-1 (Figure 8), and the highly-vesicular core (Fig. 8c) displays
661 considerable bubble coalescence as well as bubbles reaching 500 μm in diameter.

662 There is therefore a good fit between the data and model for BOMB-1, despite the model
663 using growth rates extrapolated from melt with 0.95 wt. % H_2O to considerably less H_2O-rich melt
664 (0.68 wt. % H_2O). However, caution should be applied when extrapolating bubble growth rate-

665 melt viscosity relationships across wide ranges of water concentration to account for different
666 bombs, especially when the degree of supersaturation varies greatly and spatially variable microlite
667 concentrations could introduce variably heterogeneous bubble nucleation. A future study will
668 investigate the influence of H_2O concentration on growth rate at a single temperature across a wide
669 range of H_2O concentrations.

670 Additionally, heterogeneity of H_2O concentrations over spatial scales of tens of microns to
671 centimetres within individual bombs, introduced by formation and healing of diverse fragmented
672 magma in the shallow conduit (Castro et al., 2012b; Saubin et al. 2016), can lead to spatially
673 heterogeneous vesiculation within dense melt. This phenomenon is demonstrated by the ~3 cm-
674 thick transitional zone between the dense margin and inflated core of BOMB-1, which corresponds
675 to the modelled "transition" zone (Fig. 8d; 9), in which intermediate vesicularity between core and
676 margin is expected. In fact, the ~3 cm thick zone is highly texturally heterogeneous, displaying
677 pale lens-shaped patches <1 to >6 cm across of similarly high vesicularity to the core, embedded
678 within dense glass more texturally similar to the margin. These textures likely correspond to clastic
679 textures in what is now a densely-welded breccia, with bubble-rich lenses representing large,
680 subtly more water-rich clasts within a fine-grained, more degassed matrix, a transient textural
681 phase recorded within another Chaitén bomb (Saubin et al. 2016). This phase of highly patchy
682 post-fragmentation vesiculation, with strong spatial variation in bubble growth rate, can become
683 largely overprinted in bomb centres by vesicle growth and coalescence, obscuring an important
684 intermediate phase of vesiculation. In a similar manner, potentially abundant healed clastic
685 textures in highly inflated pumices may remain largely unrecognised, even though there is
686 increasing evidence for the pyroclastic origin of dense obsidian (Castro et al., 2014; Gardner et al.,
687 2017).

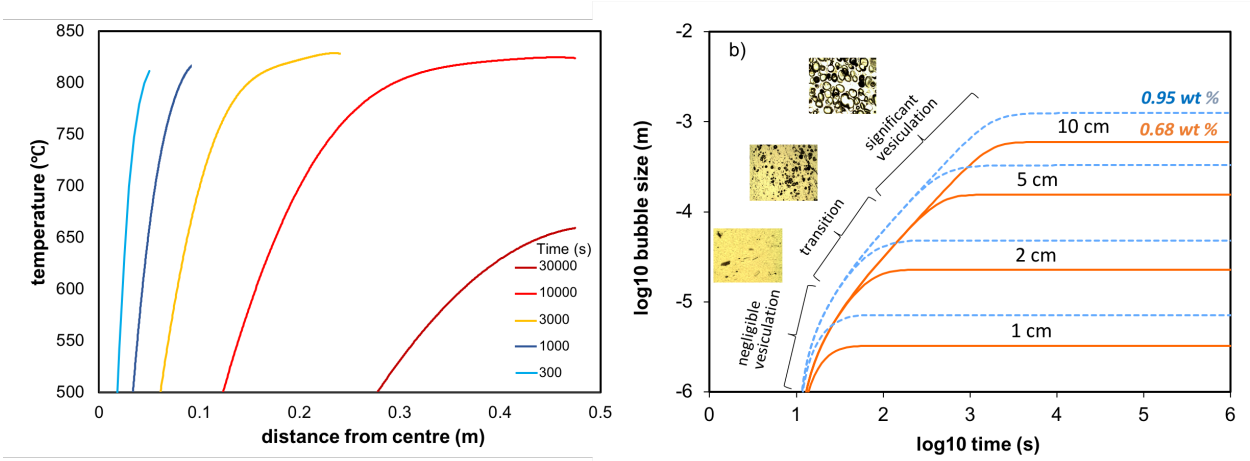

688

689 *Figure 9. (a) Temperature at different times as a function of distance from bomb edge, (b) modelled*
690 *bubble sizes over time at between 1 cm and 10 cm from the bomb margin using two different water*
691 *contents. Negligible bubble growth is expected within approximately 2 cm of the bomb margin.*

692

693 ## 5. CONCLUSIONS

694

695 The experiments conducted have allowed the two-dimensional observation of in-situ bubble
696 growth in rhyolite. Our study has shown that rate of bubble growth is strongly related to
697 temperature and melt viscosity, where $V_r = 5.57\times10^{-7}e^{0.016T}$ and $V_r = 3270.26e^{-1.117\eta}$. This simple,
698 empirically-derived relationship facilitates modelling of evolving vesicularity within rhyolitic
699 bombs, in the absence of applied shear stresses. We find that post fragmentation bubble growth
700 can occur fast enough to promote the formation of dense bubble packing associated with foam
701 textures in bombs and pyroclasts from Vulcanian type events. The efficiency of bubble growth at
702 comparatively low pressure changes is important to consider in models of conduit fragmentation
703 and degassing which often neglect the role of post-fragmentation bubble growth in cooling
704 pyroclasts. The vesiculation of bombs is not always complete upon fragmentation in the shallow
705 conduit or after a dome collapse event (Giachetti et al., 2010; Saubin et al., 2016). Instead, post-

fragmentation vesiculation may occur (e.g., Castro et al., 2012b) dependent on heat retention and H_2O concentration and presence of melt, creating textural diversity in pyroclasts with contrasting post-fragmentation thermal histories. It is important that future interpretive studies of rhyolitic pumice consider the potential for post-fragmentation vesiculation to ensure that the pre-fragmentation bubble population is not misrepresented (Giachetti et al., 2010; Saubin et al., 2016). Our quantification of vesicle growth rates for a rhyolitic bomb with approximately 1 wt.% water indicate relatively rapid growth at eruptive temperatures, with foaming over a timescale of approximately 60 seconds.

ACKNOWLEDGEMENTS

We thank the editor and three anonymous reviewers for insightful comments that helped improved the manuscript. We also thank Heidy Mader, Thomas Giachetti and Heather Wright for helpful comments on an earlier version of the manuscript. JB acknowledges a Masters scholarship from Lancaster University, Fondecyt project 11190143 and FONDAP project 15090013. HT and JO were respectively supported by a Royal Society University Research Fellowship and an AXA Postdoctoral Research Fellowship. JMC was supported by the VAMOS research centre. We thank Debbie Hurst for assistance with FTIR analysis.

REFERENCES

Applegarth, L.J., Tuffen, H., James,M.J., Pinkerton, H., Cashman, K.V. (2012) Direct observations of degassing induced crystallisation in basalts. *Geology.* **41**. 243-246

Bagdassarov, N.S., Dingwell, D.B., Wilding, M.C. (1996) Rhyolite magma degassing: an experimental study of melt vesiculation. *Bulletin of volcanology.* **57**, 587-601

Baker, D.R., Brun, F., O'shaughnessy, C., Mancini, L., Fife, J.L. and Rivers, M., 2012. A four-dimensional X-ray tomographic microscopy study of bubble growth in basaltic foam. *Nature Communications*, *3*(1), pp.1-8.

Bai, L., Baker, D.R. and Rivers, M., 2008. Experimental study of bubble growth in Stromboli basalt melts at 1 atm. *Earth and Planetary Science Letters*, *267*(3-4), pp.533-547.

Burgisser, A., and J. E. Gardner (2005), Experimental constraints on degassing and permeability in volcanic conduit flow, Bull. Volcanol., 67, 42–56.

Carslaw, H. S., & Jaeger, J. C. (1959). Conduction of heat in solids. Oxford: Clarendon Press, 1959, 2nd ed., 1.

Castro, J.M and Dingwell, D. (2009) Rapid ascent of rhyolitic magma at Chaiten volcano, Chile. *Nature.* **461** doi:10.1038/nature08458

Castro, J.M., Burgisser, A., Schipper, C.I., Mancini, S. (2012a) Mechanisms of bubble coalescence in silicic magmas. *Bulletin of Volcanology*. **74**: 2339-2352.

Castro, J.M., Cordonnier, B., Tuffen, H., Tobin, M.J., Puskar, L., Martin, M.C., Bechtel, H.A. (2012b) The role of melt-fracture degassing in defusing explosive rhyolite eruptions at volcán Chaitén. Earth and Planetary Science Letters. **333-334**: 63-69.

Castro, Jonathan M., Ilya N. Bindeman, Hugh Tuffen, and C. Ian Schipper. "Explosive origin of silicic lava: textural and δD–H2O evidence for pyroclastic degassing during rhyolite effusion." *Earth and Planetary Science Letters* 405 (2014): 52-61.

Clarke B., Calder, E.S., Dessalegn, F., Fontijn, K., Cortés, J.A., Naylor, M., Butler, I., Hutchison, W., Yirgu, G. (2019). Fluidal pyroclasts reveal the intensity of peralkaline rhyolite pumice cone eruptions. *Nature Communications* https://doi.org/10.1038 /s41467-019-09947-8

Dingwell, D.B. and Webb, S.L., 1989. Structural relaxation in silicate melts and non-Newtonian melt rheology in geologic processes. *Physics and Chemistry of Minerals*, *16*(5), pp.508-516.

Dingwell, D (1998) The glass transition in hydrous granitic melts: *Phys. Earth Planet. Inter.* **107**: 1-3

Dixon, J.E., Leist, L., Langmuir, C. and Schilling, J.G., 2002. Recycled dehydrated lithosphere observed in plume-influenced mid-ocean-ridge basalt. *Nature*, *420*(6914), pp.385-389.

Einstein, A (1911). Berichtigung zu meiner Arbeit: Eine neue Bestimmung der Moleküldimensionen, Ann. Phys. 34, 591-592.

Forte, P. and Castro, J.M., (2019). H_2O-content and temperature limit the explosive potential of rhyolite magma during Plinian eruptions. Earth and Planetary Science Letters, 506, pp.157-167.

Gardner, J.E., Thomas, R.M.E., Jaupart, C., Tait, S (1996) Fragmentation of magma during volcanic plinian eruptions. *Bulletin of volcanology,* **58**, 144-162

Gardner, J.E., Hilton, M., Carrol, M.R (1999) Experimental constraints on degassing magma: Isothermal bubble growth during continuous decompression from high pressure. *Earth and planetary science letters* **168**: 201-218

Gardner, J.E., Hilton, M., Carroll, M.R. (2000) Bubble growth in highly viscous silicate melts during continuous decompression from high pressure. *Geochimica et cosmochimica acta.* **64**, 1473-1483

Gardner, J.E. and Denis, M.H., 2004. Heterogeneous bubble nucleation on Fe-Ti oxide crystals in high-silica rhyolitic melts. *Geochim. Cosmochim. Acta*, **68**(17): 3587-3597.

Gardner, J E. 2007a. Bubble coalescence in rhyolitic melts during decompression from high pressure, *Journal of Volcanology and Geothermal Research,* **166.3**, 161-176.

Gardner, J. E. 2007b. Heterogeneous bubble nucleation in highly viscous silicate melts during instantaneous decompression from high pressure. *Chemical geology*, **236**, 1-12.

Gardner, J.E., Llewellin, E.W., Watkins, J.M. and Befus, K.S., 2017. Formation of obsidian pyroclasts by sintering of ash particles in the volcanic conduit. Earth and Planetary Science Letters, 459, pp.252-263.

Giachetti, T., Druitt, T.H., Burgisser, A., Arbaret, L., Galven, C. (2010) Bubble nucleation, growth and coalescence during the 1997 Vulcanian explosions of Soufriere Hills Volcano, Montserrat. *Journal of Volcanology and Geothermal research.* **193**, 215-231

781 Giordano, D., Nichols, A.R. and Dingwell, D.B., 2005. Glass transition temperatures of natural
782 hydrous melts: a relationship with shear viscosity and implications for the welding
783 process. *Journal of Volcanology and Geothermal Research*, *142*(1-2), pp.105-118.

784 Giordano, D., Russell, J.K., Dingwell, D.B. (2008) Viscosity of magmatic liquids: A model. *Earth*
785 *and planetary science letters.* **271**, 123-134

786 Gonnermann, H.M. and Manga, M., 2007. The fluid mechanics inside a volcano. *Annu. Rev. Fluid*
787 *Mech.*, *39*, pp.321-356.

788 Halliwell, S. (2014) Insights into melt fracture degassing and vesiculation histories of a Chaiten
789 volcanic bomb. MSc dissertation, Lancaster University, 28pp.

790 Hajimirza, S., Gonnermann, H.M. and Gardner, J.E., 2020. Eruptive dynamics in Plinian silicic
791 eruptions. Eartharxiv.

792 Hajimirza S, Gonnermann HM, Gardner JE, Giachetti T., 2019. Predicting homogeneous bubble
793 nucleation in rhyolite. JGR Solid Earth 124:2395–2416

794 Hamada, M., Laporte, D., Cluzel, N., Koga, K.T. and Kawamoto, T (2010). Simulating bubble
795 number density of rhyolitic pumices from Plinian eruptions: constraints from fast decompression
796 experiments. *Bulletin of Volcanology*, 72(6), pp.735-746.

797 Hoblitt, R. P., & Harmon, R. S. (1993). Bimodal density distribution of cryptodome dacite from
798 the 1980 eruption of Mount St. Helens, Washington. *Bulletin of Volcanology*, **55(6)**, 421-437.

799 Hodder, A. P. W. (1978). Refractive index and hydration of rhyolitic glass from Holocene tephras,
800 North Island, New Zealand. *New Zealand Journal of Geology and Geophysics*, **21(2)**, 155-166.

801 James, M. R., and S. Robson (2014), Sequential digital elevation models of active lava flows from
802 ground-based stereo time-lapse imagery, ISPRS-J. *Photogramm. Remote Sens*., **97**, 160-170,
803 doi:10.1016/j.isprsjprs.2014.08.011.

804 Kaminski, E and Jaupart, C (1997) Expansion and quenching of vesicular magma fragments in
805 Plinian eruptions. *Journal of Geophysical Research.* **102**. 187-203

Kennedy, B.M., Wadsworth, F.B., Vasseur, J., Schipper, C.I., Jellinek, A.M., von Aulock, F.W., Hess, K.U., Russell, J.K., Lavallée, Y., Nichols, A.R. and Dingwell, D.B (2016). Surface tension driven processes densify and retain permeability in magma and lava. *Earth and Planetary Science Letters*, **433**, 116-124.

Larsen, J.F. and Gardner, J.E., 2000. Experimental constraints on bubble interactions in rhyolite melts: implications for vesicle size distributions. *Earth and Planetary Science Letters*, *180*(1-2), pp.201-214.

Leschik, M., G. Heide, G. H. Frischat, H. Behrens, M. Wiedenbeck, N. Wagner, K. Heide, H. Geißler, and U. Reinholz. 2004. Determination of H2O and D2O contents in rhyolitic glasses. *Physics and Chemistry of Glasses-European Journal of Glass Science and Technology Part B* **45**, 238-251.

Lavallée, Y., Dingwell, D.B., Johnson, J.B., Cimarelli, C., Hornby, A.J., Kendrick, J.E., von Aulock, F.W., Kennedy, B.M., Andrews, B.J., Wadsworth, F.B. and Rhodes, E (2015). Thermal vesiculation during volcanic eruptions. *Nature*, **528**, 544-547.

Lui, Y and Zhang, Y. (2000) Bubble growth in rhyolitic melt. *Earth and planetary science letters.* **181**, 251-264

Lyakhovsky, V., Hurwitz, S., Navon, O (1996) Bubble growth in rhyoltic melts: experimental and numerical investigation. *Bulletin of Volcanology*. **58**: 19-32

Mangan, M., & Sisson, T. (2000). Delayed, disequilibrium degassing in rhyolite magma: decompression experiments and implications for explosive volcanism. *Earth and Planetary Science Letters*, **183**(3), 441-455.

Masotta, M., Ni, H. and Keppler, H., 2014. In situ observations of bubble growth in basaltic, andesitic and rhyodacitic melts. *Contributions to Mineralogy and Petrology*, *167*(2), p.976.

McIntosh, I. M., Llewellin, E. W., Humphreys, M. C. S., Nichols, A. R. L., Burgisser, A., Schipper, C. I., & Larsen, J. F. (2014). Distribution of dissolved water in magmatic glass records growth and resorption of bubbles. *Earth and Planetary Science Letters*, **401**, 1-11.

833 Mourtada-Bonnefoi, C.C and Laporte, D. (2004) Kinetics of bubble nucleation in a rhyolitic melt:
834 an experimental study of the effect of ascent rate. *Earth and planetary sciences.* **218**, 521-537

835 Mueller, S., Scheu, B., Spieler, O. and Dingwell, D.B., 2008. Permeability control on magma
836 fragmentation. *Geology*, *36*(5), pp.399-402.

837 Murase, T and McBirney, A.R. (1973) Properties of some common igneous rocks and their melts
838 at high temperatures. *Geological society of America bulletin.* **84**, 3563-3592

839 Navon, O., Chekhmir, A., Lyakhovsky, V. (1998) Bubble growth in highly viscous melts: theory,
840 experiments, and autoexplosity of dome lavas. *Earth and planetary science letters.* **160**, 763-776

841 Newman, S., Stolper, E. M., & Epstein, S. (1986). Measurement of water in rhyolitic glasses--
842 calibration of an infrared spectroscopic technique. *American Mineralogist*, ***71*(11)**, 1527-41.
843

844 Newman, S. and Lowenstern, J.B., 2002. VolatileCalc: a silicate melt–H2O–CO2 solution model
845 written in Visual Basic for excel. *Computers & Geosciences*, *28*(5), pp.597-604.

846 Okumura, S., & Nakashima, S. (2005). Molar absorptivities of OH and H2O in rhyolitic glass at
847 room temperature and at 400 600° C. *American Mineralogist*, **90(2-3)**, 441-447.

848 Okumura, S., Nakamura, M., Takeuchi, S., Tsuchiyama, A., Nakano, T., & Uesugi, K. (2009).
849 Magma deformation may induce non-explosive volcanism via degassing through bubble networks.
850 *Earth and Planetary Science Letters*, **281**, 267-274.

851 Okumura, S., Nakamura, M., Nakano, T., Uesugi, K., & Tsuchiyama, A. (2010). Shear
852 deformation experiments on vesicular rhyolite: Implications for brittle fracturing, degassing, and
853 compaction of magmas in volcanic conduits. *Journal of Geophysical Research*, **115**. Doi:
854 10.1029/2009JB006904

855 Owen, J., Tuffen, H. and McGarvie, D.W., 2012. Using dissolved H 2 O in rhyolitic glasses to
856 estimate palaeo-ice thickness during a subglacial eruption at Bláhnúkur (Torfajökull,
857 Iceland). *Bulletin of volcanology*, *74*(6), pp.1355-1378.

858 Owen, J., Tuffen, H., McGarvie, D.W. (2013) Pre-eruptive volatile content, degassing paths and
859 depressurisation explaining the transition in style at the subglacial rhyolitic eruption of Dalakvísl,
860 South Iceland. Journal of Volcanology and Geothermal Research **258**, 143-162.

861 Proussevitch, A.A., Sahagian, D.L., Anderson, A.T. (1993a) Dynamics of diffusive bubble growth
862 in magmas: Isothermal case. *Journal of geophysical research*. **98**. 283-307

863 Proussevitch, A.A., Sahagian, D.L., Kutolin, V.A. (1993b) Stability of foams in silicate melts.
864 *Journal of Volcanology and Geothermal research*. **59**, 161-178.

865 Proussevitch, A.A and Sahagian, D.L (1996) Dynamics of coupled diffusive and decompression
866 bubble growth prior to volcanic eruption. *Journal of Geophysics. Res.* **101**. 17447-17456

867 Proussevitch, A.A and Sahagian, D.L. (1998) Dynamics and energetics of bubble growth in
868 magmas: Analytical formulation and numerical modelling. *Journal of geophysical research.* **103**,
869 18223-18251.

870 Polacci, M., Arzilli, F., La Spina, G., Le Gall, N., Cai, B., Hartley, M.E., Di Genova, D., Vo, N.T.,
871 Nonni, S., Atwood, R.C. and Llewellin, E.W., 2018. Crystallisation in basaltic magmas revealed
872 via in situ 4D synchrotron X-ray microtomography. *Scientific reports*, *8*(1), pp.1-13.

873 Romine, W.L., Whittington, A.G., Nabelek, P.I., Hofmeister, A.M., 2012. Thermal diffusivity of
874 rhyolitic glasses and melts: effects of temperature, crystals and dissolved water. Bull. Volcanol.
875 74, 2273–2287. https://doi.org/10.1007/s00445-012-0661-6

876 Roscoe, R (1952). The viscosity of suspensions of rigid spheres, Br. J. Appl. Phys. 3. 267-269.

877 Roscoe, R (1953). Suspensions, Flow Properties of Disperse Systems, North-Holland, NewYork,

878 Ryan, A.G., Russell, J.K., Hess, K.U., Phillion, A.B. and Dingwell, D.B., 2015. Vesiculation in
879 rhyolite at low H2O contents: A thermodynamic model. Geochemistry, Geophysics, Geosystems,
880 16(12), pp.4292-4310.

881 Sahagian, D.L. and Proussevitch, A.A. (1996) Thermal effects of magma degassing. *Journal of*
882 *Volcanology and Geothermal research.* 74, 19-38.

883 Saubin, E., Tuffen, H., Gurioli, L., Owen, J., Castro, J.M., Berlo, K., McGowan, E., Schipper, C.I.
884 and Wehbe, K., (2016). Conduit Dynamics in Transitional Rhyolitic Activity Recorded by
885 Tuffisite Vein Textures from the 2008–2009 Chaitén Eruption. Frontiers in Earth Science, 4.

886 Sparks, R.S.J. (1978) The dynamics of bubble formation and growth in magmas: A review and
887 analysis. *Journal of Volcanology and Geothermal research.* 3, 1-37

888 Soriano, C., Giordano, D., Galindo, I., Hürlimann, M. and Ardia, P., 2009. Giant gas bubbles in a
889 rheomorphic vent fill at the Las Cañadas caldera, Tenerife (Canary Islands). *Bulletin of*
890 *volcanology*, *71*(8), p.919.

891 Stasiuk, M.V., Barclay, J., Carroll, M.R., Jaupart, C., Ratté, J.C., Sparks, R.S.J. and Tait, S.R.,
892 1996. Degassing during magma ascent in the Mule Creek vent (USA). *Bulletin of*
893 *Volcanology*, *58*(2-3), pp.117-130.

894 Stevenson, R.J., Dingwell, D.B., Webb, S.L. and Bagdassarov, N.S., 1995. The equivalence of
895 enthalpy and shear stress relaxation in rhyolitic obsidians and quantification of the liquid-glass
896 transition in volcanic processes. *Journal of Volcanology and Geothermal Research*, *68*(4), pp.297-
897 306.

898 Toramaru, A (1989), Vesiculation processes and bubble size distributions in ascending magmas
899 with constant velocities, J. Geophys. Res., 94, 17,523–17,542.

900 Toramaru, A (1995), Numerical study of nucleation and growth of bubbles in viscus magmas, J.
901 Geophys. Res., 100, 1913–1931.

902 Thomas, N., Jaupart, C., Vergniolle, S (1994) On the vesicularity of pumice. *Journal of*
903 *Geophysical Research,* **99**, 15633-15644

904 Turcotte, D.L., Schubert, G., 1982. *Geodynamics*. John Wiley and Sons, New York, 450 pp.

905 von Aulock, F. W., Kennedy, B. M., Schipper, C. I., Castro, J. M., Martin, D. E., Oze, C., Watkin,
906 J.M., Wallace, P.J., Puskar, L., Begue, F., Nichols, A.R.L., Tuffen, H. (2014). Advances in Fourier
907 transform infrared spectroscopy of natural glasses: From sample preparation to data analysis.
908 *Lithos*, **206**, 52-64.

von Aulock, F.W., Kennedy, B.M., Maksimenko, A., Wadsworth, F.B. and Lavallée, Y., (2017). Outgassing from open and closed magma foams. Frontiers in Earth Science, 5, p.46.

Watkins, J., Manga, M., and DePaolo, D. (2012) Bubble geobarometry: A record of pressure changes, degassing, and regassing at Mono Craters, California, Geology, doi: 10.1130/G33027.1.

Webb, S., 1997. Silicate melts: Relaxation, rheology, and the glass transition. *Reviews of Geophysics*, *35*(2), pp.191-218.

Wright, H.M.N., Cashman, K.V., Rosi, M., and Cioni, R. (2007). Breadcrust bombs as indicators of Vulcanian eruption dynamics at Guagua Pichincha volcano, Ecuador. *Bull. Volcanol*. **69**: 281-300

Zhang, Y., Stolper, E.M., Wasserburg, G.J. (1991) Diffusion of water in rhyolite glasses. *Geochemica et cosmochimica acta*. **55**. 441-456

Zhang, Y (1999) H_2O in Rhyolitic glasses and melts: Measurement, speciation, solubility, and diffusion. *Reviews in Geophysics*, **37**: 493-516

SUPPLEMENTARY DATA:

Supplement 1. Composition of Chaiten obs 3 rhyolite glass sample

Oxide	**(wt.%)**
SiO2	76.10
TiO2	0.13
Al2O3	12.00
FeO(T)	1.27
MnO	0.06
MgO	0.28
CaO	1.41
Na2O	4.00
K2O	2.98
P2O5	0.04
H2O	0.95
F2O-1	0.00
Total	99.84

Supplement 2. Summary of results, bubble number density increase is shown for each sample. Nucleation rates and growth rates are calculated using the methods previously discussed.

Sample no.	**Initial BND mm^{-3} (n_i)**	**Final BND mm^{-3} (n_f)**	**% increase**	**Maximum Diameter (mm) (d_{max})**	**Avg Growth rate (mm s^{-1}) (V_r)**	**Maximum Nucleation Rate (mm^{-3} s^{-1}) (I_{max})**	**Avg Nucleation Rate (mm^{-3} s^{-1}) (I)**
875	560	1360	143	101	1.27	24	15
875_R	467	1167	150	119	1.72	14	10
850	1120	1800	61	152	0.94	12	4
825	300	767	156	207	0.67	15	7
825_R	3040	3380	11	101	0.57	4	2
775	1000	1217	22	102	0.37	1	1

775_R	1816	1994	10	139	0.24	6	5
725	311	311	0	80	0.02		
625	367	367	0	52	None		
575	800	800	0	65	None		

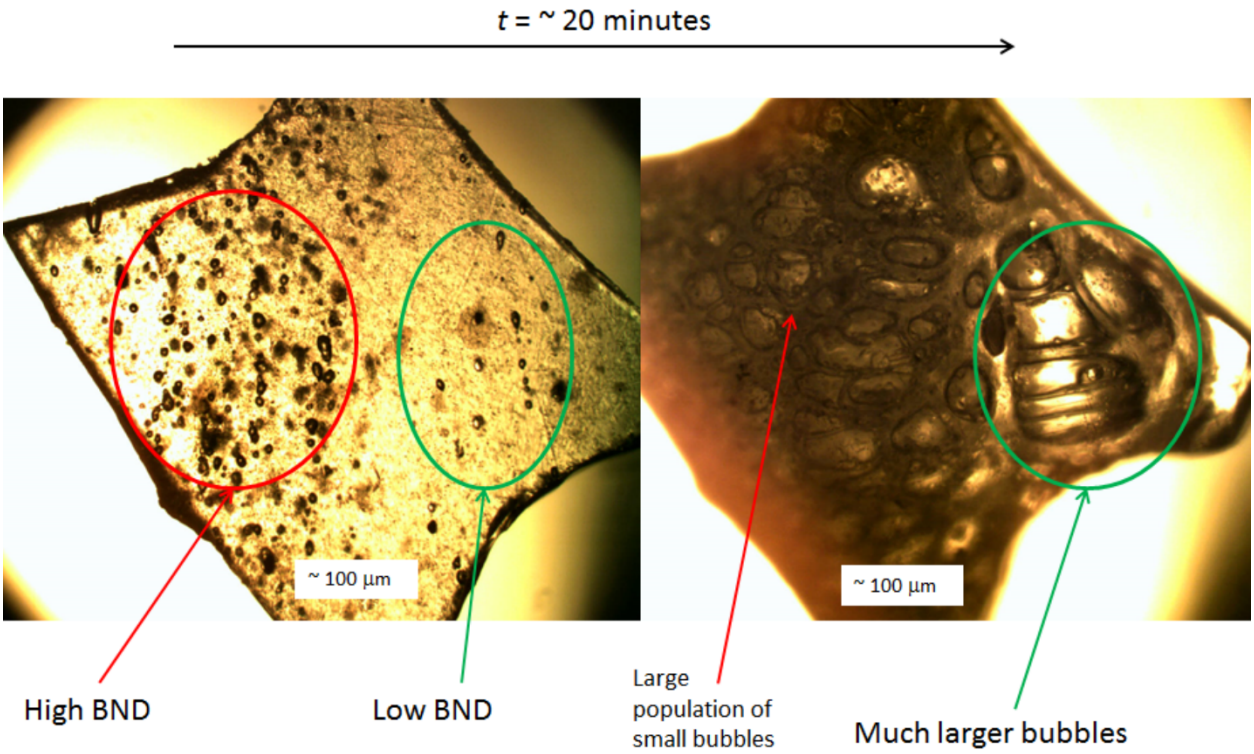

Supplement 3. Chaiten rhyolite imaged at x10 magnification over a period of ~20 minutes. A contrast exists between areas of high and low initial vesicularity and the final bubble size of populations in these two areas. In an area of high BND, growth of vesicles has been prohibited causing a population of many small bubbles. In contrast the bubbles in an area of low BND have been able to grow and deform significantly more.

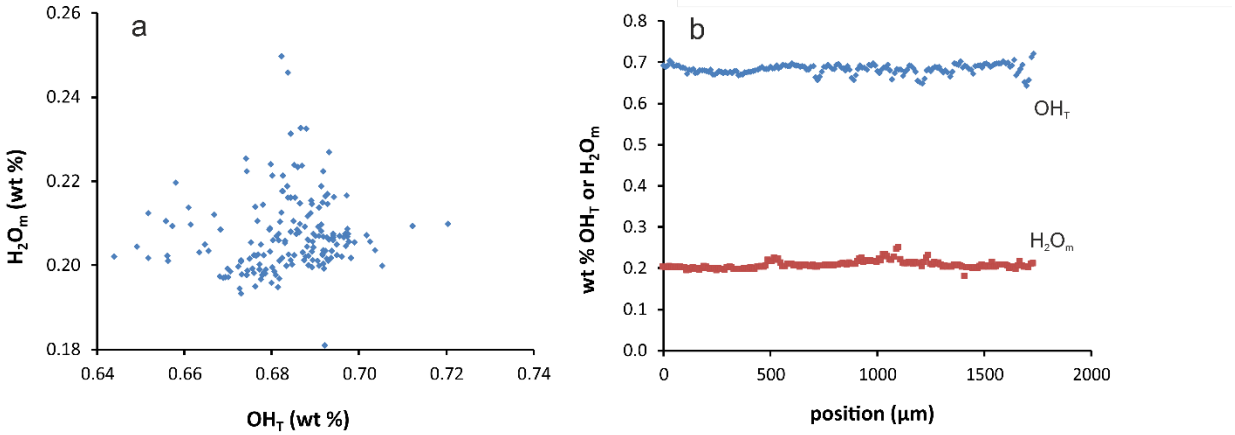

940

941 *Supplement 4. FTIR data showing the H_2O_m and OH_T contents of BOMB-1.*

942

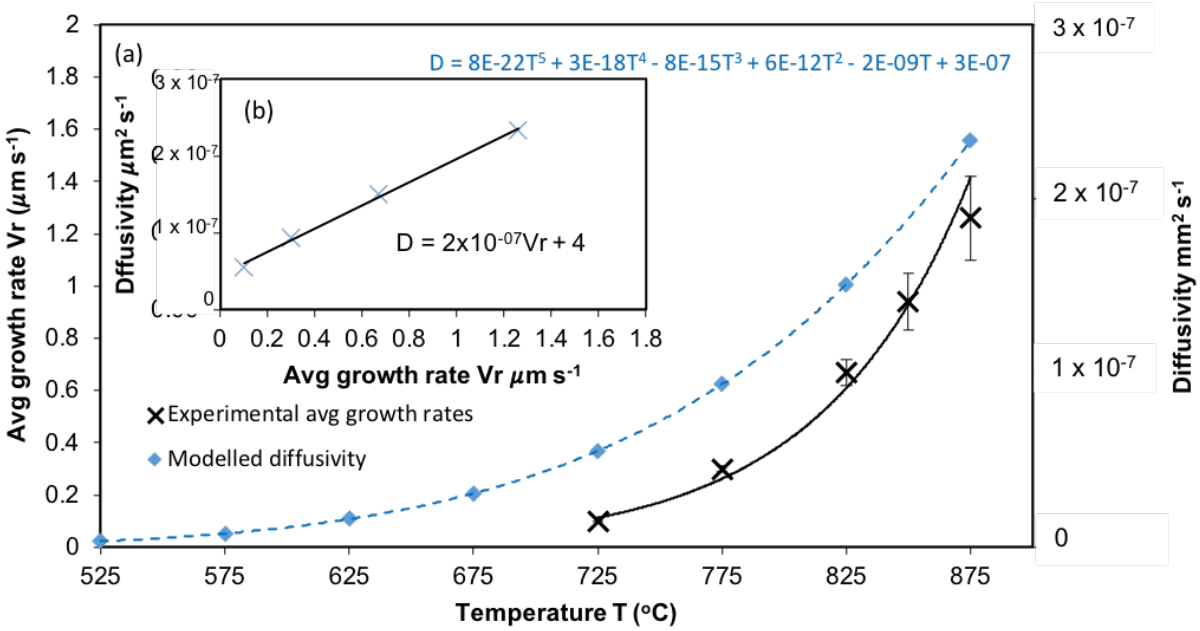

943

944 *Supplement 5. Relationship between diffusivity and temperature is similar to that of growth rate*
945 *and temperature (a), showing an exponential relationship where diffusivity = exp (0.0119T) and*
946 *Vr = exp (0.0169T). As such the relationship between modelled diffusivity (D) and growth rate*
947 *(Vr) is linear (b).*

948